Article

Human organoids with an autologous tissue-resident immune compartment

https://doi.org/10.1038/s41586-024-07791-5

Received: 31 August 2023

Accepted: 5 July 2024

Published online: 14 August 2024

Open access

Check for updates

Timothy Recaldin[1,6], Linda Steinacher[1,2,3,6], Bruno Gjeta[2,4,6], Marius F. Harter[2,5,6], Lukas Adam[2], Kristina Kromer[2], Marisa Pimentel Mendes[1], Marina Bellavista[2], Mikhail Nikolaev[2], Giacomo Lazzaroni[1], Rok Krese[2], Umut Kilik[2,4], Doris Popovic[2], Bilgenaz Stoll[2], Régine Gerard[2], Michael Bscheider[1], Marc Bickle[2], Lauriane Cabon[2]✉, J. Gray Camp[2]✉ & Nikolche Gjorevski[2]✉

The intimate relationship between the epithelium and immune system is crucial for maintaining tissue homeostasis, with perturbations therein linked to autoimmune disease and cancer[1–3]. Whereas stem cell-derived organoids are powerful models of epithelial function[4], they lack tissue-resident immune cells that are essential for capturing organ-level processes. We describe human intestinal immuno-organoids (IIOs), formed through self-organization of epithelial organoids and autologous tissue-resident memory T (T_{RM}) cells, a portion of which integrate within the epithelium and continuously survey the barrier. T_{RM} cell migration and interaction with epithelial cells was orchestrated by T_{RM} cell-enriched transcriptomic programs governing cell motility and adhesion. We combined IIOs and single-cell transcriptomics to investigate intestinal inflammation triggered by cancer-targeting biologics in patients. Inflammation was associated with the emergence of an activated population of $CD8^+$ T cells that progressively acquired intraepithelial and cytotoxic features. The appearance of this effector population was preceded and potentiated by a T helper-1-like $CD4^+$ population, which initially produced cytokines and subsequently became cytotoxic itself. As a system amenable to direct perturbation, IIOs allowed us to identify the Rho pathway as a new target for mitigation of immunotherapy-associated intestinal inflammation. Given that they recapitulate both the phenotypic outcomes and underlying interlineage immune interactions, IIOs can be used to study tissue-resident immune responses in the context of tumorigenesis and infectious and autoimmune diseases.

Organoids originating from adult stem cells model important aspects of human physiology and have applications in research related to genetic disorders, infectious disease, cancer, regenerative medicine and drug discovery[4]. However, they are epithelial-only structures, whereas native organs comprise multiple other compartments, including specialized immune cells that have essential roles in homeostasis and disease[5,6]. For example, the intestinal mucosal immune system—the largest pool of immune cells in the human body[7]—ensures homeostasis by perpetual policing of the interface between the intestinal barrier and luminal contents. Disruption of intestinal immune function can lead to various pathologies, including persistent infections and autoimmune and even malignant disease[1–3,8]. Whereas intestinal organoids can accurately model the differentiation and function of epithelial cell types[9–11], they fall short in capturing key aspects of intestinal (patho)physiology owing to the absence of a tissue-specific immune compartment[12].

To address these shortcomings, adult or induced pluripotent stem cell-derived organoids have been co-cultured with blood-derived innate or adaptive immune cells[13–15]. However, the incorporation of a mucosal lymphocyte compartment has proven elusive. One recent study described the generation of gut-associated lymphoid tissue in induced pluripotent stem cell-derived human intestinal organoids following transplantation in humanized mice[16]. Although representing an important advance, the in vivo formation of immune tissue removes the advantage of organoids as being controllable in vitro systems. Similarly, fetal intestinal organoids have been co-cultured with effector memory T cells but no model exists that includes a true adult tissue-resident lymphocyte compartment with the memory features acquired over the course of a human lifespan[17].

We created a tractable intestinal immuno-organoid (IIO) model containing a tissue-resident and autologous immune compartment starting from readily available adult human tissue samples (Fig. 1a). We benchmarked cell states in IIOs through comparison with reference atlases using single-cell transcriptomes, and used IIOs to recapitulate and investigate drug-induced intestinal inflammation.

In our efforts to introduce a relevant lymphocyte compartment into organoids, we focus on tissue-resident memory T (T_{RM}) cells—antigen-experienced T cell populations, which take permanent

[1]Roche Innovation Center Basel, Roche Pharma Research and Early Development, Basel, Switzerland. [2]Institute of Human Biology (IHB), Roche Pharma Research and Early Development, Basel, Switzerland. [3]Hannover Medical School, Institute of Immunology, Hannover, Germany. [4]University of Basel, Basel, Switzerland. [5]Gustave Roussy Cancer Campus, University Paris-Saclay, Paris, France. [6]These authors contributed equally: Timothy Recaldin, Linda Steinacher, Bruno Gjeta, Marius F. Harter. ✉e-mail: lauriane.cabon@roche.com; gray.camp@roche.com; nikolche.gjorevski@roche.com

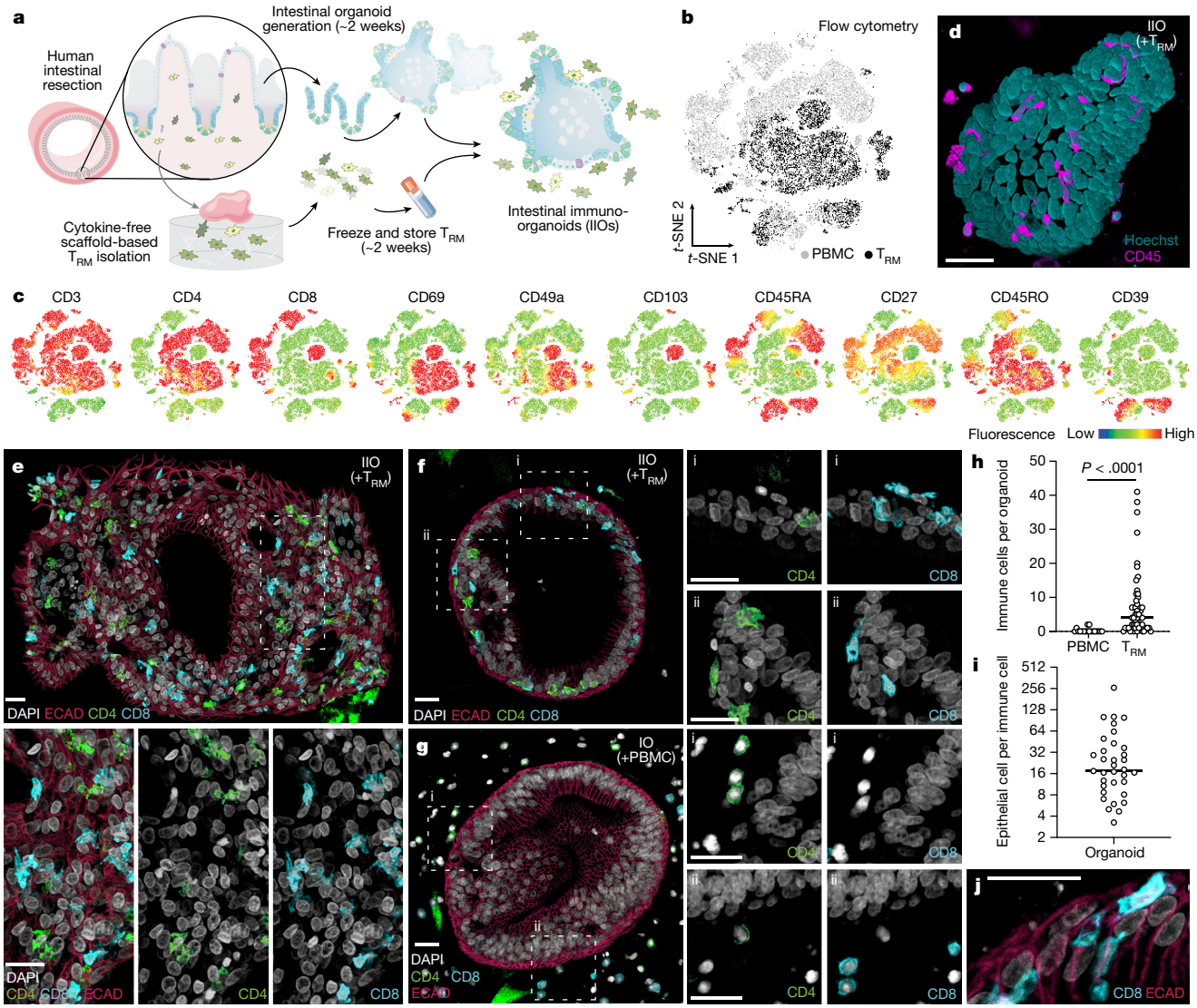

Fig. 1 | Intestine-derived T_{RM} cells integrate homeostatically into autologous organoids to form IIOs. a, Schematic overview of establishment of autologous IIOs (adapted with permission from ref. 60). **b**,**c**, Flow cytometry-based, *t*-distributed stochastic neighbour-embedding (*t*-SNE) analysis of donor-matched gut T_{RM} cell and circulating PBMC T cell subgroups based on surface marker expression, derived from one donor and representative of six biological replicates. *t*-SNE plot coloured according to original source of T cells (**b**; light grey for PBMCs and black for T_{RM} cells), and expression of ten individual markers of naivety, memory and tissue residency (**c**). **d**, Fluorescent live image 24 h following IIO co-culture set-up (nuclei, teal; T cells, pink). Similar images were observed with four biological replicates. **e**–**g**, mIF staining of cultures 24 h following co-culture with autologous T_{RM} cells (**e**,**f**) or PBMCs (**g**). Intestinal organoids highlighted by E-cadherin$^+$ (ECAD) epithelium (red). CD4$^+$ (green) and CD8$^+$ (turquoise) T_{RM} cells integrated within larger (**e**) or smaller (**f**) organoids whereas blood-derived CD4$^+$ and CD8$^+$ T cells surrounded the organoid (**g**). Box i and box ii highlight the presence (**f**) or absence (**g**) of immune cell integration into two representative regions (i and ii) of the epithelium. **e**–**g**, miF images representative of three independent biological replicates. IO, intestinal organoid. **h**, Immune cell count detected per organoid, each data point representing an individual organoid; $n = 18$ for PBMCs and $n = 54$ for T_{RM} cells, two-tailed Mann–Whitney test. **i**, Ratio of epithelial to immune cells within each organoid ($n = 35$), 24 h following organoid supplementation with autologous T_{RM} cells. **h**,**i**, Data represent the collation of two independent IIO cultures. Similar results were observed in three biological replicates. **j**, Elongated flossing T cell inserting between basal and lateral epithelial cell junctions. Scale bars, 25 µm (**d**–**g**,**j**).

residence in the intestinal mucosa, providing frontline defence against pathogens[6]. Given the absence of recirculation, they are an appropriate lymphocyte type for stable incorporation into organoid models. Furthermore, their memory character ensures functionality in the absence of antigen-presenting cells, lymphoid structures and the remaining immune cell recirculation apparatus. Because human T_{RM} cells are difficult to incorporate into in vitro systems owing to their poor viability following enzymatic removal from tissue[18,19], we adapted an enzyme-free, scaffold-based crawl-out protocol to isolate large numbers of intestinal immune cells[20] (Fig. 1a). Even in the complete absence of cytokine or T cell receptor (TCR) stimulation, our approach liberated significantly more cells than enzymatic digestion-based protocols, meanwhile retaining similar proportions of immune cell types (Extended Data Fig. 1a,b). Flow cytometry analysis showed that the isolated cells expressed T_{RM} cell markers pertinent to the intestine, including CD161 (IL-17A production[21]) and CD117 (Notch signalling[22], encoded by *KIT*; Extended Data Fig. 1c), as well as surface molecules associated with tissue retention (CD69 (ref. 23)), extracellular matrix association (CD49a[24], encoded by *ITGA1*) and epithelial cell integration (CD103 (ref. 25), encoded by *ITGAE*), all of which were barely detectable on blood-derived T cells (Fig. 1b,c). We deemed the lack of cytokine exposure crucial for retaining the tissue-like physiological properties of intestine-derived lymphocytes, as demonstrated by a change in key activation markers following exposure to IL-2 and IL-15 (Extended

Data Fig. 1d). Our gut-derived T cells were exclusively memory cells ($CD45RO^+CD45RA^-$) with limited capacity for lymph node homing ($CCR7^-$), and these expressed high levels of the IL-7 receptor CD127 (Extended Data Fig. 1e). The final pool of isolated immune cells sometimes contained myeloid cells and B lymphocytes, largely dependent on the tissue specimen itself (Extended Data Fig. 1b). Nonetheless, because the overwhelming majority (mean 84.5%) were T_{RM} cells, we use the abbreviation T_{RM} cells to refer to the pool of immune cells harvested from human intestinal samples.

We generated organoids and T_{RM} cells from human intestinal specimens, additionally collecting matched peripheral blood mononuclear cells (PBMCs) from the same donor. Once established, organoids were combined with T_{RM} cells or PBMCs within a three-dimensional extracellular matrix (ECM) at physiologically relevant cellular concentrations[26] and in the absence of external stimulation. Confocal microscopy showed that, following co-culture, T_{RM} cells were viable and closely associated with organoids (Fig. 1d and Supplementary Video 1). To examine organoid–T_{RM} cell interactions in detail we generated histological sections of the models and visualized both epithelial and immune cells (Fig. 1e–g). We found that, whereas PBMCs occupied the ECM space with no apparent interaction with epithelial cells (Fig. 1g), a subpopulation of T_{RM} cells infiltrated the organoids and integrated within the epithelial barrier in the absence of stimulation, resembling the behaviour of intestinal intraepithelial lymphocytes (IELs)[27] (Fig. 1e,f,h). We estimated a median integration ratio of 16 epithelial cells per one immune cell (Fig. 1i)—highly similar to observations in the intestinal tract of healthy humans[28]. IELs showed an elongated morphology of up to around 60 µm in length (Fig. 1j and Extended Data Fig. 1f), around ten times the length of a naive blood-derived T cell[29] and reminiscent of the 'flossing' behaviour described for murine IELs imaged in vivo[27]. With low-level cytokine support, immune-organoid cultures could be maintained for at least 14 days (Extended Data Fig. 1g–j). This model provides an example of self-organization between human immune cells and epithelial organoids to form an organoid system with a tissue-resident immune compartment. We termed these IIOs; henceforth we use IIOs to refer to organoids co-cultured with autologous gut-derived T_{RM} cells and containing integrated IELs.

Elegant in vivo studies have dissected the dynamics of murine TCRγδ IELs and their interaction with the intestinal epithelium[27]. Owing to their poor survival in vitro, similar studies of human IEL behaviour have proved challenging[18,19] and the mechanisms driving human-specific IEL integration are poorly elucidated. To understand how T_{RM} cells and IELs integrate with intestinal epithelial cells in vitro, and how they differ from PBMCs in that regard, we used single-cell RNA sequencing (scRNA-seq) for analysis of IIO cultures derived from three different small intestinal samples. We ran scRNA-seq 24 h following IIO initiation because the integration of T_{RM} cells is complete at this time point, as demonstrated by longitudinal flow cytometry experiments showing stable T_{RM} cell composition and activation profiles within the first 4 days of co-culture, in the absence of any treatment (Extended Data Fig. 2a). We compared these with matched PBMCs co-cultured with organoids, and included gut-derived T_{RM} cells cultured in Matrigel alone as an additional control (Fig. 2a). Heterogeneity analysis and visualization using uniform manifold approximation and projection (UMAP) embedding demonstrated the presence of 10 epithelial and 14 immune cell clusters across all three donors (Extended Data Fig. 2b–e). Epithelial cell proportions and gene expression were generally stable between IIOs and organoids cultured with PBMCs, although we observed that the presence of T_{RM} cells led to a significant upregulation of *ID3* and *HES1* in IIO epithelial stem cells (Extended Data Fig. 2f,g), genes associated with intestinal stem cell maintenance[30,31] and microbial defence[32]. We focused our analysis on T cells (and closely related natural killer (NK) cells), given their predominance within the tissue-derived population, and identified three distinct populations representing 15 clusters of blood-derived naive, blood- and gut-derived effector cells and gut-derived T_{RM} cells (Fig. 2b,c, Extended Data Fig. 2h and Supplementary Table 1). Further interrogation of T cell populations based on previously published markers demonstrated that T_{RM} cells cultured alone or within IIOs, unlike their matched blood-derived counterparts, were transcriptomically defined by: (1) the absence of receptors necessary for lymph node homing (*SELL*, *CCR7*), (2) intrinsically high expression of intestinal homing and integration factors (*ITGA1*, *CCR9*, *JAML*) and (3) a complete absence of cytotoxic granules (*GZMB*, *GZMK*, *GNLY*) (Fig. 2c and Supplementary Table 2). We observed representation across each cluster from all three donors, demonstrating the consistency and reproducibility of the different immune states (Fig. 2d). To identify the main functional differences between T_{RM} cells and PBMCs we considered the top differentially regulated T_{RM} cell genes (Fig. 2e). Gene Ontology analysis suggested an enrichment in transcriptomic programs related to immune cell chemotaxis and migration within T_{RM} cells compared with PBMCs (Fig. 2f), which may explain their propensity for integration within the epithelium. Indeed, live-imaging experiments in which donor-matched gut T_{RM} cells and blood T cells were tracked over time (Fig. 2g and Supplementary Videos 2 (T_{RM} cells) and 3 (blood T cells)) showed a marked difference in morphology and migratory behaviour between the two populations. Whereas blood T cells were largely static and round (Supplementary Video 3), T_{RM} cells exhibited elongated shapes and migrated dynamically within both the epithelial layers and ECM (Fig. 2g,h and Supplementary Video 2). We note that intestinal organoids are a sterile system and that the introduction of luminal microorganisms may lead to altered modes of migration and interaction with the epithelium, as described in mice[27].

For assessment of the impact of the epithelium on T_{RM} cells within IIOs, relative to T_{RM} cells cultured alone, we reconstructed a neighbourhood enrichment score (integration index) of T cells based on connectivity in canonical correlation analysis space. Comparison of neighbourhoods composed almost exclusively of IIO-derived T_{RM} cells (bin 5) with those composed of T_{RM} cells cultured alone (bin 3) demonstrated enriched expression of genes associated with cell motility and cytoskeletal rearrangement (*ANXA1*, *ANXA2*, *LGALS3*, *S100A6*, *S100A10*, *S100A11*) (Extended Data Fig. 2i–k). Conversely, T_{RM} cells cultured alone showed heightened expression of genes required to navigate into the gut and around the ECM (*JAML*, *SOS1*, *CD96*, *ITGA1*), but not of those to integrate into the epithelium (Extended Data Fig. 2k). This indicated that the epithelium reinforced and amplified the intraepithelial character of T_{RM} cells, presumably through the frequent cell-to-cell contacts we observed and describe in Fig. 1.

Next we tested whether differential transcriptomes and migration behaviours between T_{RM} cells and PBMCs would translate into differences in effector function. In particular, we investigated whether IIOs could recapitulate clinical toxicities associated with cancer immunotherapy manifesting as severe intestinal inflammation[33,34]. We focused on solitomab—a bispecific T cell engager intended to cross-link activated T cells with solid tumours via the epithelial cell adhesion molecule (EpCAM)—which induced aggressive unintentional intestinal inflammation in patients, preventing escalation to therapeutic doses and ultimately leading to program termination[34]. Given the rapid onset of side effects, IELs localized within the basolateral epithelial junctions have been hypothesized to elicit this damage. To assess whether IEL-containing IIOs could have predicted targeting of the heatlthy epithelium we treated IIOs with an EpCAM-targeting, T cell-bispecific (TCB) molecule at clinically relevant concentrations[34]. Unlike organoids cultured with PBMCs, IIOs were targeted in a TCB dose-dependent manner at concentrations as low as 40 pg ml^{-1} and as early as 8 h following treatment, as demonstrated by the detection of caspase 3/7 (Fig. 3a–c and Extended Data Fig. 3a). We assessed T cell behaviour at early (5 h), middle (24 h) and late (48 h) time points by digestion and staining of IIOs for surface and intracellular markers of T cell activation and cytotoxicity (Extended Data Fig. 3b). Identification

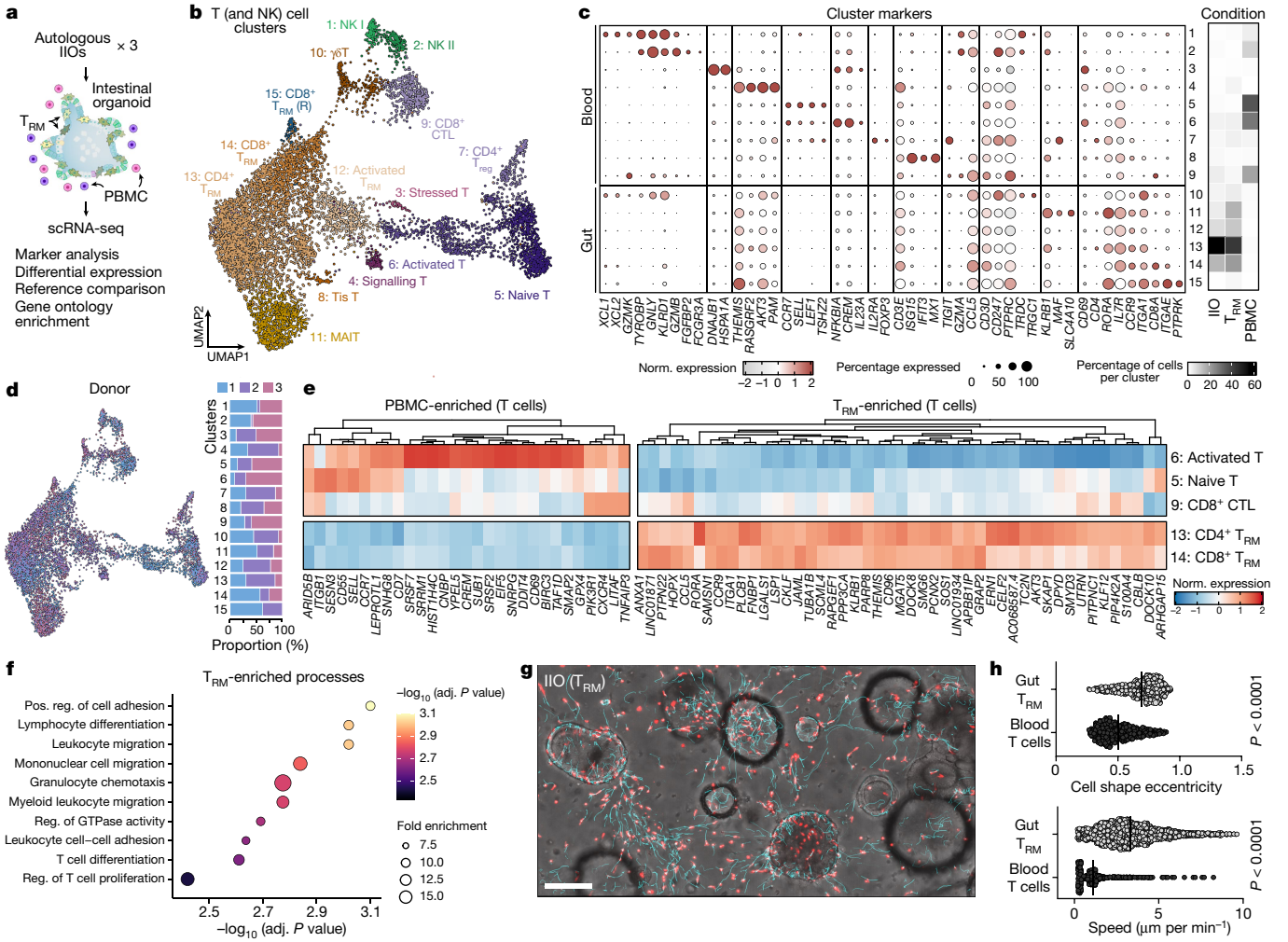

Fig. 2 | Tissue-resident transcriptomic signatures and migratory behaviour underlie T_{RM} cell epithelial insertion and IIO formation. a, Overview of single-cell transcriptome analysis of organoids containing patient-matched T_{RM} cells and PBMCs. Data were generated from T_{RM} cells alone (T_{RM}), organoids containing T_{RM} cells (IIO) and organoids containing PBMCs (PBMC) from three small intestine donors (one jejunum, one duodenum, one undefined small intestine). Organoid schematic adapted with permission from ref. 60, human schematic adapted from ref. 61. **b**, Integrated UMAP embedding of transcriptome data from immune cells of each condition, showing 15 distinct cell clusters (colours, numbers) labelled based on analysis of marker genes (see Extended Data Fig. 2 for the entire dataset). R, resting. **c**, Dotplot summarizing marker gene expression across different clusters. Heatmap sidebar shows proportional distribution of each condition across clusters. **d**, Left, immune cell UMAP with each cell coloured by donor; right, stacked barplot showing donor cell proportion in each cluster in which each column sums to 100. **e**, Heatmap representing genes with enriched expression in PBMCs (left) or T_{RM} cells (right). **f**, Plot showing significantly enriched Gene Ontology biological processes of genes marking $CD8^+$ and $CD4^+$ T_{RM} cell clusters. Enrichment *P* value was generated using hypergeometric test with Bonferroni's multiple-hypothesis correction. **g**, Images showing migration analysis derived from IIO time-lapse imaging. Tracks are shown in cyan, immune cells in red. Data quantified in **h**. **h**, Comparison of T_{RM} cell and blood-derived T cell shape (top) and speed (bottom) from 42 min time-lapse imaging of IIO and organoid + T cell cultures. Two-tailed Mann–Whitney test. Each dot represents a detected cell and is the collation of duplicate cultures from one representative experiment. Cell shape eccentricity, $n = 471$ for gut T_{RM} cells and $n = 593$ for blood T cells; motility, $n = 2{,}335$ for gut T_{RM} cells and $n = 866$ for blood T cells. Similar results were observed with three biological replicates. Scale bar, 100 μm.

of effector populations, based on the expression of TNF, IFNγ and granzyme B (Gzmb), showed that over 90% of responding cells were intestinal T_{RM} cells (Extended Data Fig. 3c). Furthermore, we observed that T_{RM} cells began expressing CD38, HLA-DR and Ki67—activation and proliferation markers found on cells that drive colitis-like pathology in vivo[35,36] (Extended Data Fig. 3d). Supernatant analysis reinforced these findings, with key cytokines TNF, IFNγ, Gzmb, IL-2 and GM-CSF all more detectable in T_{RM} cell IIO cultures (Extended Data Fig. 3e)

We found that, although circulating memory cells were more potent than their naive counterparts, responses were significantly weaker than those of matched T_{RM} cells (Extended Data Fig. 3f). Within T_{RM} cells, $CD103^-$ (lamina propria) and $CD103^+$ (intraepithelial) fractions triggered equivalent epithelial targeting (Extended Data Fig. 3g,h), which was also maintained in longer-term IIO cultures with TCB added 10 days following co-culture (Extended Data Fig. 3i).

To investigate whether T_{RM} cell-mediated inflammatory responses might affect circulating immune cells, we supplemented IIOs with PBMCs and treated them with TCB (Extended Data Fig. 4a). The presence of T_{RM} cells led to enhanced PBMC integration within organoids compared with organoid + PBMCs cultured in the absence of T_{RM} cell (Extended Data Fig. 4b). Furthermore, we noted synergistic induction of myeloid-associated cytokines IL-1β, IL-6 and IL-8 in IIO cultures supplemented with PBMCs, suggesting that a tissue-resident immune compartment can potentiate responses of peripheral immune cells within the system (Extended Data Fig. 4b–d).

The mechanisms of severe rapid-onset toxicities caused by T cell-targeted therapies are unclear, because patients who experience them are not biopsied in the acute phase. IIOs, which we show can recapitulate aspects of clinical outcomes, provide the opportunity for in-depth analysis of the underlying immunological events. We used scRNA-seq to interrogate the transcriptomic dynamics underlying TCB-dependent T_{RM} cell activity at the onset (4 h) and peak (48 h) of epithelial cell targeting. Lymphocyte populations within the integrated dataset were annotated using differential gene expression, together with previously published signatures and surface markers[35,37–40], showing predominantly T cell, but also macrophage and B cell, populations in this particular specimen (Fig. 3d,e and Supplementary Tables 1 and 2). TCB treatment induced a shift in proportions of both T and B cell states relative to the non-targeting control (Fig. 3f), driven by the emergence of several effector populations at both time points. Particularly prominent at 4 h was a $CD4^+$ T helper 1-like (T_H1) population (c9) (Fig. 3d–f), characterized by rapid induction of *TNF* and *IFNG* signalling that became downmodulated over time (Fig. 3g,h). At 48 h we observed the emergence of an activated $CD8^+$ IEL population (c5) (Fig. 3d–f) expressing genes related to cytotoxicity (such as *GZMB*), TCR signalling and T cell migration (Fig. 3g,h). Concurrently, a population of cycling (*MKI67*-expressing) $CD4^+$ T cells (c12) and an activated population of B cells (c11) appeared whereas the regulatory T cell population (c1) diminished (Fig. 3d–g). Importantly, key gene expression changes detected by scRNA-seq were mirrored by changes at the protein level, as recorded by flow cytometry (Fig. 3i). We observed early induction of TNF in $CD4^+$ cells at 4 h (corresponding to c9) whereas cytotoxic Gzmb was upregulated at 48 h, in line with the appearance of c5. Likewise, Ki67 was strongly upregulated within a subset of $CD4^+$ cells at 48 h, co-occurring with the appearance of c12 within the scRNA-seq analysis. IIO cell heterogeneity dynamics bear striking similarities to those observed within primary samples from patients experiencing spontaneous and immune checkpoint inhibitor (ICI)-induced intestinal inflammation. For example, the emergence of a cytotoxic $CD8^+$ T cell population was one of the main features of patients experiencing ICI-induced colitis[35,36]. Likewise, regulatory T cell transition towards pathogenic cytokine production and the appearance of activated IFNγ-responsive B cell populations are well-described features of colitis pathophysiology[41–43]. These similarities suggest that IIOs may be used to recapitulate and study intestinal inflammation in a tractable in vitro setting.

Next we charted the activation dynamics of the clinically relevant $CD8^+$ T cell population. Using Diffusion Maps[44], we computed a pseudotemporal ordering of populations c3 and c5 (Fig. 4a and Extended Data Fig. 5a) and observed a marked correlation with experimental time (Fig. 4b and Extended Data Fig. 5b). This reconstructed activation trajectory allowed for characterization of the transcriptional dynamics underlying $CD8^+$ T_{RM} cell activation (Extended Data Fig. 5c). We observed induction of glycolytic regulators *ENO1* and *HIF1A* and suppression of *TCF7* and ZBTB32 (refs. 45–48) that probably facilitate the appropriate metabolic profile for full activation. Simultaneously *CCL5*, important for immune cell recruitment[49], and *IL7R*, which mediates cytotoxic activation[50], correlated with the induction of cytotoxicity genes *GZMA*, *GZMB* and *NKG7*. Sequencing of biopsies of patients suffering from drug-induced colitis demonstrated the presence of both cytotoxic (CTL) and IEL $CD8^+$ T cell populations[35]. By cross-referencing TCB-treated IIOs to this dataset, we found that IIO $CD8^+$ T cells acquired gene signatures related to a cytotoxic and IEL state, mirroring those observed in clinical samples (Extended Data Fig. 5d,e). The concurrent increase in lymphocyte–epithelium association and cytotoxicity may underlie the severe clinical adverse events triggered by these molecules.

Aside from $CD8^+$ CTLs, other populations showed clinically relevant dynamics of early- versus late-transcriptional hallmarks. Consistent with clinical reports[51], a T_H1 population (c9) shifted from a cytokine-producing to a cytotoxic state (Fig. 4c and Extended Data Fig. 5f). Likewise, the early IFN-responsive B cell population (c11) showed a transcriptional landscape distinct from that of the late, activated state (Fig. 4d and Extended Data Fig. 5g). We performed a receptor–ligand pairing analysis and investigated how activated phenotypes might emerge via intercellular signalling (Fig. 4e). Our model implicates T_H1 cells (c9) as a major organizational hub, instructing B cells (c11) and $CD8^+$ T cells (c5) through the secretion of numerous signalling factors (Fig. 4f and Extended Data Fig. 5h,i). Meanwhile, the $CD4^+$ T cell (c9) expression of *TNF* corresponded to increased *CALM1* expression in activated $CD8^+$ IELs (c5), potentially augmenting TCR-induced calcium signalling and T cell maturation[52] (Fig. 4f and Extended Data Fig. 5j). Ligand-to-target signalling models and network propagation analysis[53] reaffirmed these observations, suggesting that T_H1-produced *IFNG* may mediate B cell activation whereas *TNF* and *IL2* act in tandem to orchestrate cytotoxic $CD8^+$ cell maturation (Extended Data Fig. 5h,i).

A key advantage of human model systems is their amenability to experimental manipulation as a means of defining the roles of putative regulators. Given the effectiveness of TNF-blocking antibodies in the treatment of autoimmune disease, and the early induction of TNF in our model (Fig. 3h,i), we investigated its role in the promotion of differentiation and activation. In silico perturbation analysis predicted that the complete removal of *TNF* from IIOs would prevent T_{RM} cell activation (Fig. 4g). Antibody neutralization of TNF using adalimumab in IIOs following TCB treatment confirmed this forecast, significantly reducing the T_{RM} cell expression of key activation and differentiation markers ICAM-1, 4-1BB, CD25 and Gzmb (Extended Data Fig. 6a). Furthermore, expression of CCL2, a chemokine expressed by the epithelium in response to inflammation[54], as well as epithelial cell apoptosis itself, were significantly reduced (Fig. 4h–j and Extended Data Fig. 6b). This effect appeared to be mediated by TNF effects on T_{RM} cells rather than direct cytotoxicity to the epithelium, because direct organoid exposure to recombinant TNF had no impact on epithelial caspase signal (Extended Data Fig. 6c,d). Having confirmed the impact of neutralization of a clinically validated pathway, we used the transcriptomic data defining T_{RM} cell identity (Fig. 2) to suggest new factors that could be manipulated to quell inflammation. Given the rapid T_{RM} cell locomotion within the ECM, we hypothesized that T cell motility might, in part, be responsible for the outcome. To test this hypothesis we used the ROCK1/2 inhibitor (ROCKi) Y-27632 to abrogate cell motility within TCB-treated IIOs. Strikingly, we found that ROCK inhibition reduced epithelial cell apoptosis even more efficiently than TNF blockade (Fig. 4h–j), simultaneously suppressing T_{RM} cell motility (Supplementary Video 4 and Extended Data Fig. 6e) and the induction of T cell activation markers and cytolytic molecules such as perforin and Gzmb (Extended Data Fig. 6f). Intracellular staining showed that TNF induction was also suppressed but overall T cell viability was unchanged (Extended Data Fig. 6g,h). In addition to TNF- and Rho-mediated signalling, the transcriptomic and ligand–receptor analyses shown provide a wide range of putative targets for managing inflammation, which are worth investigation in future studies.

Immune checkpoint inhibitors such as anti-CTLA-4 and anti-PD-1 induce durable responses in a wide range of human cancers but simultaneously trigger enterocolitic symptoms in 10–15% of patients by exacerbation of contemporaneous immune responses to gut microflora or viral infections[35,55–57]. Because $CD8^+$ T_{RM} cells have been described as key drivers of this pathology, we tested whether our IIO cultures could recapitulate this phenomenon. We pretreated T_{RM} cell or matched PBMC controls with allogeneic dendritic cells to recapitulate the role on antigen-presenting cells, either in the presence or absence of anti-CTLA-4 (ipilimumab) and anti-PD-1 (nivolumab), and then exposed them to organoids. Although we did not detect

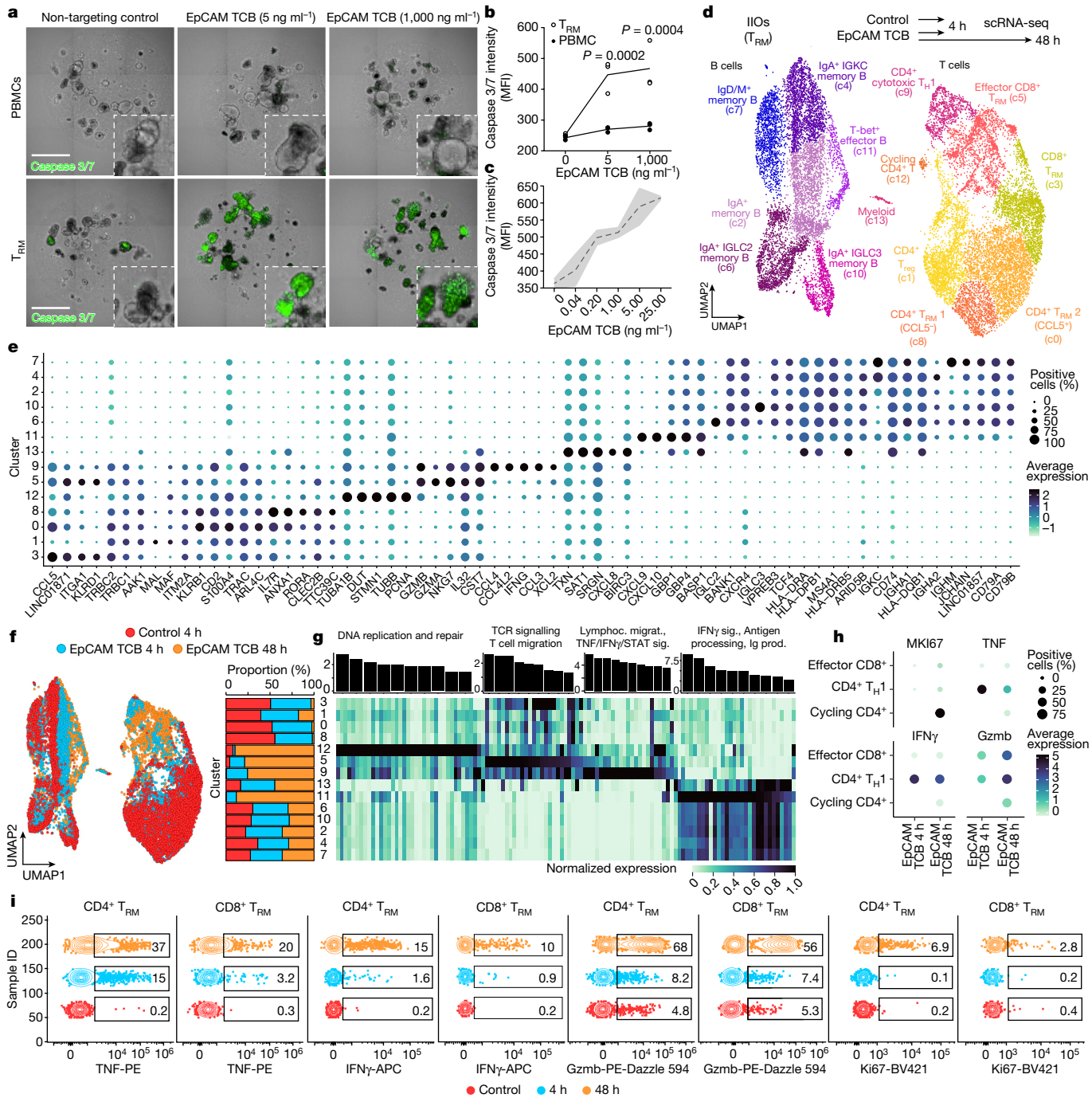

Fig. 3 | IIOs recapitulate clinically manifested intestinal inflammation associated with TCB. a, Representative images examining induction of green caspase 3/7 signal within IIO co-cultures 24 h following supplementation with EpCAM TCB. **b**, Quantification of caspase 3/7 signal from **a**. Two-way analysis of variance (ANOVA) with Sidak's multiple-comparisons test. Triplicate IIO cultures representative of experiments performed with three independent biological donors. MFI, mean fluorescence intensity. **c**, Quantification of caspase 3/7 signal in IIO co-cultures treated for 72 h across a range of EpCAM TCB. Two independent IIO cultures were run across a six-dose titration of EpCAM TCB; mean (black line) and s.d. (grey shading). **d**, Single-cell transcriptomic profiles of gut-derived immune cells from IIO model were integrated and grouped into 14 distinct cell states as represented by colours in the UMAP embedding. Organoid schematic adapted with permission from ref. 60. **e**, Dotplot summarizing the expression patterns of representative genes across the clusters identified in **d**. **f**, Integrated UMAP embedding (left) and proportional distribution (right) of gut-derived immune cells from IIO model, coloured by treatment and profiling time. **g**, Barplot showing significantly enriched Gene Ontology biological processes for activated cell states (top) and heatmap showing average expression profiles of corresponding associated genes (bottom). **h**, Dotplot summarizing the expression pattern of representative genes involved in proliferation, signalling and cytotoxicity in activated T cell populations, as captured by scRNA-seq snapshots at different time points and under various treatment conditions. **i**, Flow cytometry plots visualizing expression of TNF, IFNγ, Gzmb and Ki67 across different time points within $CD4^+$ and $CD8^+$ T_{RM} cells isolated from IIO cultures. Representative of five biologically independent experiments. Scale bars, 1 mm.

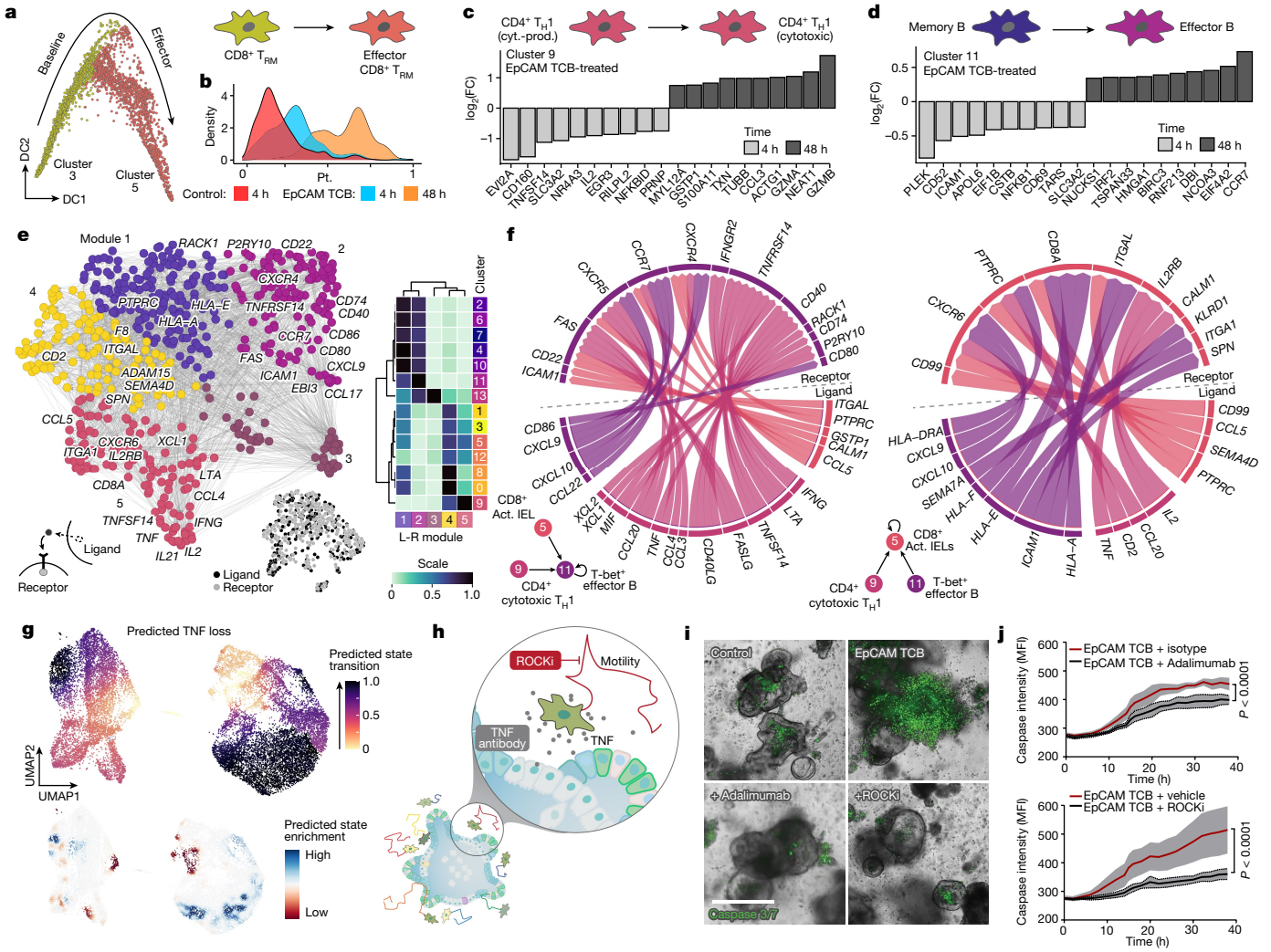

Fig. 4 | Transcriptomic analyses elucidate the immune dynamics underlying TCB-mediated inflammation and help identify mitigation strategies. **a**, $CD8^+$ T cell activation in the IIO model was analysed using diffusion maps. Plot represents $CD8^+$ T cells on the first two diffusion components (DCs), coloured by cell state. **b**, Density plot showing distribution of $CD8^+$ T cells along the reconstructed pseudotime (*x* axis) grouped by treatment condition and time point. **c**,**d**, Barplot showing differentially expressed genes for $CD4^+$ cytotoxic T_H1 population (c9) (**c**) and T-bet$^+$ effector B cells (c11) (**d**) at 4 h (light grey) and 48 h (dark grey) following EpCAM TCB treatment. **e**, Ligand–receptor pairing analysis of IIO immune cell populations. Ligands and receptors are coloured based on coexpression module, with some representative genes labelled. Heatmap (right) shows the average expression of each gene within a module across each cell cluster. **f**, Circle plots illustrate signalling interactions received by T-bet$^+$ effector B cells (c11) (left) and $CD8^+$ Act. IELs (c5) (right). **g**, In silico perturbation analysis simulating the loss (KO) of *TNF* in the IIO model treated with EpCAM TCB. Plots show predicted perturbation-induced state transition (top) and enrichment (bottom). **h**, Schematic of experiments performed to inhibit TNF signalling and cell migration. Organoid cartoon adapted with permission from ref. 60. **i**, Representative images showing induction of caspase 3/7 signal within IIO co-cultures 40 h following supplementation with either a non-targeting control TCB or 5 ng ml^{-1} EpCAM TCB, with or without 10 µM ROCKi or a TNF blocking antibody. **j**, Bi-hourly quantification of caspase 3/7 signal in IIO cultures; top, comparison of EpCAM TCB + isotype with EpCAM TCB + adalimumab; bottom, comparison of EpCAM TCB + vehicle with EpCAM TCB + ROCKi. Data represent mean and standard deviation (grey shading) of three independent biological replicates; two-tailed unpaired *t*-test of the area under the curve generated for each condition. Scale bar, 200 µm. FC, fold change.

changes in caspase signal (Extended Data Fig. 7a), the more sensitive lactate dehydrogenase (LDH) assay showed a statistically significant increase in signal in one of the two T_{RM} cell biological replicates treated with ICIs (Extended Data Fig. 7b). The response was associated with an increase in $CD8^+$ T_{RM} cells expressing CD38, Gzmb and Ki67 (Extended Data Fig. 7c,d), similar to the disease-driving populations described in patients[35,36]. Interestingly, both PBMCs and T_{RM} cells from either donor showed augmented activation following ICI treatment (Extended Data Fig. 7e), but the increase in LDH signal was present only under the T_{RM} cell condition in which pathogenic $CD8^+$ T cell numbers were increased (Extended Data Fig. 7c,d), suggesting that close association with the epithelium might be required for damage.

We thus describe human IIOs, comprising human intestinal epithelium and autologous T_{RM} cells, a subpopulation of which is directly integrated within the IIO epithelial barrier, as orchestrated by T_{RM} cell-enriched transcriptomic programs governing cell motility and adhesion. Crucially, IIOs formed following co-culture with T_{RM} cells but not blood-derived lymphocytes, which failed to migrate and interact with organoids. Although epithelial cell identity did not shift markedly following T_{RM} cell integration, we hypothesize that T_{RM} cells influence epithelial barrier integrity, defence and regeneration[5,6]. Given that these shifts probably manifest under conditions of challenge, adaptations to the model to allow luminal access and routine introduction of gut pathogens is an exciting area we are actively pursuing.

The inclusion of a tissue-appropriate immune compartment extends the utility of organoids beyond epithelium-centred questions. We use IIOs to recapitulate intestinal inflammation caused by TCBs. IIOs treated with TCBs undergo rapid apoptosis, consistent with early-onset diarrhoea and epithelial lesions in patients[34]. Importantly, whereas co-cultures with PBMCs have been shown to capture similar outcomes, effects occur at concentrations 1,000-fold higher than clinical doses and, even then, with a delayed onset[58]. Through dissection of the transcriptomic changes induced by TCB treatment, we show that adverse outcomes are underpinned by dynamic interlineage immune interactions that parallel mechanisms associated with checkpoint inhibitor-induced intestinal inflammation and inflammatory bowel disease[35,36,51].

Our model provides the advantages of direct perturbation and hypothesis testing. Whereas multiomic analyses of primary patient samples provide rich catalogues of differences between normal and diseased states, the exact roles of differentially regulated parameters are difficult to ascertain. Having demonstrated that IIOs respond to clinically effective mitigation strategies, we use them to identify new approaches for the management of TCB-mediated toxicities. We find that blocking of T_{RM} cell motility through the Rho pathway helps dampen inflammation. Intriguingly, small molecules that target this pathway are being developed as fibrosis inhibitors for inflammatory bowel disease[59]. Bearing in mind that our simple model recapitulates both the phenotypic outcomes and cellular interactions that mediate them, IIOs can help investigate tissue-resident immune responses in contexts far beyond drug-induced inflammation, including tumorigenesis and infectious and autoimmune diseases.

Online content

Any methods, additional references, Nature Portfolio reporting summaries, source data, extended data, supplementary information, acknowledgements, peer review information; details of author contributions and competing interests; and statements of data and code availability are available at https://doi.org/10.1038/s41586-024-07791-5.

1. Girardi, M. et al. Regulation of cutaneous malignancy by gammadelta T cells. *Science* **294**, 605–609 (2001).
2. Mayassi, T. et al. Chronic inflammation permanently reshapes tissue-resident immunity in celiac disease. *Cell* **176**, 967–981 (2019).
3. Dart, R. J. et al. Conserved gammadelta T cell selection by BTNL proteins limits progression of human inflammatory bowel disease. *Science* **381**, eadh0301 (2023).
4. Schutgens, F. & Clevers, H. Human organoids: tools for understanding biology and treating diseases. *Annu. Rev. Pathol.* **15**, 211–234 (2020).
5. Gray, J. I. & Farber, D. L. Tissue-resident immune cells in humans. *Annu. Rev. Immunol.* **40**, 195–220 (2022).
6. Masopust, D. & Soerens, A. G. Tissue-resident T cells and other resident leukocytes. *Annu. Rev. Immunol.* **37**, 521–546 (2019).
7. Holmgren, J. & Czerkinsky, C. Mucosal immunity and vaccines. *Nat. Med.* **11**, S45–S53 (2005).
8. Puel, A. et al. Chronic mucocutaneous candidiasis in humans with inborn errors of interleukin-17 immunity. *Science* **332**, 65–68 (2011).
9. Beumer, J. et al. Enteroendocrine cells switch hormone expression along the crypt-to-villus BMP signalling gradient. *Nat. Cell Biol.* **20**, 909–916 (2018).
10. Sato, T. et al. Paneth cells constitute the niche for Lgr5 stem cells in intestinal crypts. *Nature* **469**, 415–418 (2011).
11. Grun, D. et al. Single-cell messenger RNA sequencing reveals rare intestinal cell types. *Nature* **525**, 251–255 (2015).
12. Bar-Ephraim, Y. E., Kretzschmar, K. & Clevers, H. Organoids in immunological research. *Nat. Rev. Immunol.* **20**, 279–293 (2020).
13. Jowett, G. M. et al. Organoids capture tissue-specific innate lymphoid cell development in mice and humans. *Cell Rep.* **40**, 111281 (2022).
14. Noel, G. et al. A primary human macrophage-enteroid co-culture model to investigate mucosal gut physiology and host-pathogen interactions. *Sci. Rep.* **7**, 45270 (2017).
15. Tominaga, K. et al. Generation of human intestinal organoids containing tissue-resident immune cells. *Gastroenterology* **162**, S57 (2022).
16. Bouffi, C. et al. In vivo development of immune tissue in human intestinal organoids transplanted into humanized mice. *Nat. Biotechnol.* **41**, 824–831 (2023).
17. Schreurs, R. et al. Human fetal TNF-alpha-cytokine-producing CD4(+) effector memory T cells promote intestinal development and mediate inflammation early in life. *Immunity* **50**, 462–476 (2019).
18. Beura, L. K. et al. Intravital mucosal imaging of CD8(+) resident memory T cells shows tissue-autonomous recall responses that amplify secondary memory. *Nat. Immunol.* **19**, 173–182 (2018).
19. Swamy, M. et al. Intestinal intraepithelial lymphocyte activation promotes innate antiviral resistance. *Nat. Commun.* **6**, 7090 (2015).
20. Clark, R. A. et al. A novel method for the isolation of skin resident T cells from normal and diseased human skin. *J. Invest. Dermatol.* **126**, 1059–1070 (2006).
21. Maggi, L. et al. CD161 is a marker of all human IL-17-producing T-cell subsets and is induced by RORC. *Eur. J. Immunol.* **40**, 2174–2181 (2010).
22. Massa, S., Balciunaite, G., Ceredig, R. & Rolink, A. G. Critical role for c-kit (CD117) in T cell lineage commitment and early thymocyte development in vitro. *Eur. J. Immunol.* **36**, 526–532 (2006).
23. Kumar, B. V. et al. Human tissue-resident memory T cells are defined by core transcriptional and functional signatures in lymphoid and mucosal sites. *Cell Rep.* **20**, 2921–2934 (2017).
24. Bank, I., Book, M. & Ware, R. Functional role of VLA-1 (CD49A) in adhesion, cation-dependent spreading, and activation of cultured human T lymphocytes. *Cell. Immunol.* **156**, 424–437 (1994).
25. Cepek, K. L. et al. Adhesion between epithelial cells and T lymphocytes mediated by E-cadherin and the alpha E beta 7 integrin. *Nature* **372**, 190–193 (1994).
26. Fu, Y. Y. et al. T cell recruitment to the intestinal stem cell compartment drives immune-mediated intestinal damage after allogeneic transplantation. *Immunity* **51**, 90–103 (2019).
27. Hoytema van Konijnenburg, D. P. et al. Intestinal epithelial and intraepithelial T cell crosstalk mediates a dynamic response to infection. *Cell* **171**, 783–794 (2017).
28. Sergi, C., Shen, F. & Bouma, G. Intraepithelial lymphocytes, scores, mimickers and challenges in diagnosing gluten-sensitive enteropathy (celiac disease). *World J. Gastroenterol.* **23**, 573–589 (2017).
29. Tasnim, H. et al. Quantitative measurement of naive T cell association with dendritic cells, FRCs, and blood vessels in lymph nodes. *Front. Immunol.* **9**, 1571 (2018).
30. Hu, L. et al. Bone morphogenetic protein 4 alleviates DSS-induced ulcerative colitis through activating intestinal stem cell by target ID3. *Front. Cell Dev. Biol.* **9**, 700864 (2021).
31. Kayahara, T. et al. Candidate markers for stem and early progenitor cells, Musashi-1 and Hes1, are expressed in crypt base columnar cells of mouse small intestine. *FEBS Lett.* **535**, 131–135 (2003).
32. Guo, X. K., Ou, J., Liang, S., Zhou, X. & Hu, X. Epithelial Hes1 maintains gut homeostasis by preventing microbial dysbiosis. *Mucosal Immunol.* **11**, 716–726 (2018).
33. Amann, M. et al. Therapeutic window of MuS110, a single-chain antibody construct bispecific for murine EpCAM and murine CD3. *Cancer Res.* **68**, 143–151 (2008).
34. Kebenko, M. et al. A multicenter phase 1 study of solitomab (MT110, AMG 110), a bispecific EpCAM/CD3 T-cell engager (BiTE(R)) antibody construct, in patients with refractory solid tumors. *Oncoimmunology* **7**, e1450710 (2018).
35. Luoma, A. M. et al. Molecular pathways of colon inflammation induced by cancer immunotherapy. *Cell* **182**, 655–671 (2020).
36. Sasson, S. C. et al. Interferon-gamma-producing CD8(+) tissue resident memory T cells are a targetable hallmark of immune checkpoint inhibitor-colitis. *Gastroenterology* **161**, 1229–1244 (2021).
37. Andreatta, M. et al. Interpretation of T cell states from single-cell transcriptomics data using reference atlases. *Nat. Commun.* **12**, 2965 (2021).
38. Szabo, P. A. et al. Single-cell transcriptomics of human T cells reveals tissue and activation signatures in health and disease. *Nat. Commun.* **10**, 4706 (2019).
39. Wang, X. et al. Reinvestigation of classic T cell subsets and identification of novel cell subpopulations by single-cell RNA sequencing. *J. Immunol.* **208**, 396–406 (2022).
40. Elmentaite, R. et al. Cells of the human intestinal tract mapped across space and time. *Nature* **597**, 250–255 (2021).
41. Hovhannisyan, Z., Treatman, J., Littman, D. R. & Mayer, L. Characterization of interleukin-17-producing regulatory T cells in inflamed intestinal mucosa from patients with inflammatory bowel diseases. *Gastroenterology* **140**, 957–965 (2011).
42. Bamidele, A. O. et al. Interleukin 21 drives a hypermetabolic state and CD4(+) T-cell-associated pathogenicity in chronic intestinal inflammation. *Gastroenterology* https://doi.org/10.1053/j.gastro.2024.01.026 (2024).
43. Castro-Dopico, T. et al. Anti-commensal IgG drives intestinal inflammation and type 17 immunity in ulcerative colitis. *Immunity* **50**, 1099–1114 (2019).
44. Haghverdi, L., Buttner, M., Wolf, F. A., Buettner, F. & Theis, F. J. Diffusion pseudotime robustly reconstructs lineage branching. *Nat. Methods* **13**, 845–848 (2016).
45. Gemta, L. F. et al. Impaired enolase 1 glycolytic activity restrains effector functions of tumor-infiltrating CD8(+) T cells. *Sci. Immunol.* https://doi.org/10.1126/sciimmunol.aap9520 (2019).
46. Finlay, D. K. et al. PDK1 regulation of mTOR and hypoxia-inducible factor 1 integrate metabolism and migration of CD8+ T cells. *J. Exp. Med.* **209**, 2441–2453 (2012).
47. Chen, Z. et al. TCF-1-centered transcriptional network drives an effector versus exhausted CD8 T cell-fate decision. *Immunity* **51**, 840–855 (2019).
48. Shin, H. M. et al. Transient expression of ZBTB32 in anti-viral CD8+ T cells limits the magnitude of the effector response and the generation of memory. *PLoS Pathog.* **13**, e1006544 (2017).
49. Zeng, Z., Lan, T., Wei, Y. & Wei, X. CCL5/CCR5 axis in human diseases and related treatments. *Genes Dis.* **9**, 12–27 (2022).
50. Micevic, G. et al. IL-7R licenses a population of epigenetically poised memory CD8(+) T cells with superior antitumor efficacy that are critical for melanoma memory. *Proc. Natl Acad. Sci. USA* **120**, e2304319120 (2023).

51. Riaz, T., Sollid, L. M., Olsen, I. & de Souza, G. A. Quantitative proteomics of gut-derived Th1 and Th1/Th17 clones reveal the presence of CD28+ NKG2D- Th1 cytotoxic CD4+ T cells. *Mol. Cell. Proteomics* **15**, 1007–1016 (2016).
52. Trebak, M. & Kinet, J. P. Calcium signalling in T cells. *Nat. Rev. Immunol.* **19**, 154–169 (2019).
53. Browaeys, R., Saelens, W. & Saeys, Y. NicheNet: modeling intercellular communication by linking ligands to target genes. *Nat. Methods* **17**, 159–162 (2020).
54. Ho, A. W., Wong, C. K. & Lam, C. W. Tumor necrosis factor-alpha up-regulates the expression of CCL2 and adhesion molecules of human proximal tubular epithelial cells through MAPK signaling pathways. *Immunobiology* **213**, 533–544 (2008).
55. Dougan, M. Checkpoint blockade toxicity and immune homeostasis in the gastrointestinal tract. *Front. Immunol.* **8**, 1547 (2017).
56. Beck, K. E. et al. Enterocolitis in patients with cancer after antibody blockade of cytotoxic T-lymphocyte-associated antigen 4. *J. Clin. Oncol.* **24**, 2283–2289 (2006).
57. Lo, B. C. et al. Microbiota-dependent activation of CD4(+) T cells induces CTLA-4 blockade-associated colitis via Fcgamma receptors. *Science* **383**, 62–70 (2024).
58. Harter, M. F. et al. Analysis of off-tumour toxicities of T-cell-engaging bispecific antibodies via donor-matched intestinal organoids and tumouroids. *Nat. Biomed. Eng*. https://doi.org/10.1038/s41551-023-01156-5 (2023).
59. Holvoet, T. et al. Treatment of intestinal fibrosis in experimental inflammatory bowel disease by the pleiotropic actions of a local Rho kinase inhibitor. *Gastroenterology* **153**, 1054–1067 (2017).
60. Gjorevski, N. et al. Tissue geometry drives deterministic organoid patterning. *Science* **375**, eaaw9021 (2022).
61. Pollen, A. A., Kilik, U., Lowe, C. B. & Camp, J. G. Human-specific genetics: new tools to explore the molecular and cellular basis of human evolution. *Nat. Rev. Genet.* **24**, 687–711 (2023).

Methods

Human samples

Human intestinal tissue samples and annotated data were obtained, and experimental procedures performed, within the framework of the non-profit foundation HTCR (Munich, Germany), including informed patient consent. The framework of the HTCR Foundation has been approved by the ethics commission of the Faculty of Medicine in the Ludwig Maximilian University (no. 025-12) and the Bavarian State Medical Association (no. 11142). Twenty-seven consenting patients underwent visceral surgery with partial resection of intestine (16 males, 11 females, age range 40–89 years; precise intestinal regions are listed in Supplementary Table 4) for various oncologic indications, including pancreaticojejunostomy due to pancreatic adenocarcinoma (example no. ICD10, codes C18.x, C24.x and C25.x). We used micro- and/or macroscopically tumour-free regions of resectates for further preparation.

Isolation of T_{RM} cells and donor-matched crypts for organoid generation

Intestinal tissue was first processed by removal of the underlying muscularis, serosa and fat from the basal side of the tissue by pinching with forceps and trimming away with scissors. The remaining mucosal tissue was washed with PBS (supplemented with penicillin (1,500 U ml^{-1}), streptomycin (1,500 µg ml^{-1}) and gentamicin (500 µg ml^{-1})) multiple times before using a scalpel to remove excess mucus from the luminal side and blood vessels from the basal side. Trimmed, cleaned tissue was then cut into square explants (approximately 5 × 5 mm^3) with a scalpel. Lymphoid follicles such as Peyer's patches were not separated from lamina propria tissue. Two methodologies were used to isolate intestinal T_{RM} cells. For the scaffold-based egression protocol (adapted from ref. 20), each explant was loaded onto a 9 × 9 × 1.5 mm^3 tantalum-coated, carbon-based scaffold (Ultramet) and cultured in 24-well plates containing 1 ml of cytokine-free cell culture medium (RPMI 1640, 10% fetal calf serum (FCS), penicillin (1,500 U ml^{-1}), streptomycin (1,500 µg ml^{-1}), gentamicin (500 µg ml^{-1}) and amphotericin (12.5 µg ml^{-1})). Twenty-four hours later, scaffolds and tissue were removed and egressed cells were harvested from the bottom of the culture well via pipetting. For the enzymatic digestion protocol, explants were digested using the Human Tumour Dissociation Kit with the gentleMACS Octo Dissociator program 37C_h_TDK_1 (Miltenyi Biotec), as per the manufacturer's instructions, reducing Enzyme R content by 80% to minimize surface antigen cleavage. Cells were then counted, phenotyped by flow cytometry and frozen before use in downstream applications. For isolation of donor-matched crypts for organoid generation, a lamelle was scraped over a 3 cm^2 piece of trimmed tissue to remove intestinal protrusions/villi. Tissue was then incubated in ice-cold PBS + 10 mM EDTA with vigorous shaking for 30 min to break down epithelial cell junctions. Tissue was retrieved and a lamelle used to scrape off crypts into DMEM-F12 1% bovine serum albumin (BSA) collection buffer. Crypts were centrifuged, resuspended in Matrigel Matrix GFR (Corning) and cultured in IntestiCult Organoid Growth Medium with 10 µM Y-27632 (STEMCELL Technologies). Absolute authentication was confirmed by expression of cell lineage-defining markers and transcriptomic analysis. All lines used in the studies were verified as negative for mycoplasma before further experimentation.

Preparation and culture of IIOs, including treatment

In-passage organoids, approximately 2 weeks to 1 month following initial isolation, were cultured for 4 days post split in IntestiCult Organoid Growth Medium and then switched to IntestiCult Organoid Differentiation Medium (STEMCELL Technologies) for 72 h to promote epithelial stem cell differentiation. On the day of co-culture set-up, medium was aspirated from the well and organoids were washed with PBS and treated with ice-cold Cell Recovery Solution (Corning) for 40 min. The solution was collected and centrifuged to harvest the liberated organoids. Donor-matched T_{RM} cells or PBMCs were thawed, combined with the liberated organoids and resuspended in either Matrigel Matrix GFR (Corning) or, if co-cultures were to be formalin fixed, a 50:50 mixture of Matrigel Matrix GF and 4 mg ml^{-1} Cultrex Rat Collagen I (R&D Systems). For time-lapse live-imaging experiments, immune cells were labelled with CellTrace Far Red or CFSE (ThermoFisher) before mixing with organoids. Organoids were used at a concentration double their standard passaging density, whereby a 20 µl dome was harvested and resuspended in 10 µl of matrix, whereas immune cells were used at a density of 15,000 mm^{-3} of resuspension volume. A 50:50 ratio of RPMI 1640 10% FCS and IntestiCult Organoid Differentiation Medium was used for culture. For assessment of TCB-based cytotoxicity, an EpCAM-CD3 bispecific antibody, or its associated non-targeting control (which contains a CD3 binder on one arm and a non-specific DP47 arm), was supplemented into the culture medium following co-culture set-up, or 10 days following co-culture set-up in the case of experiments with longer-term IIO cultures, typically at a concentration of 5 ng ml^{-1}. When used, blocking antibodies to TNF (adalimumab, InvivoGen) were added at a concentration of 1 µg ml^{-1}. To investigate the role of ROCK signalling on T_{RM} cell activation, 10 µM Y-27632 was added daily for the duration of the co-culture. For longer-term co-cultures (up to 1 month), a 50:50 ratio of RPMI 1640 10% FCS and IntestiCult Organoid Growth Medium, supplemented with IL-2 (10 IU ml^{-1}) (Roche) and IL-15 (2 ng ml^{-1}; BioLegend) was used. Medium was changed three times per week and the culture split once per week. Cultures were supplemented with 10 µM Y-27632 (STEMCELL Technologies) following splitting. For investigation of T_{RM} cell-generated inflammation to study recruitment of circulating T cells into the epithelium, CellTracker CMFDA Green (ThermoFisher) was used to stain PBMCs at a final working concentration of 1 µM. For single T_{RM} cell–organoid and PBMC–organoid co-cultures, the density of immune cells previously described was used. However, for T_{RM} cell–PBMC–organoid co-culture, both T_{RM} cell and PBMC compartments were seeded at 15,000 cells mm^{-3} of resuspension volume.

Flow cytometry analysis of immune-organoids

Triplicate wells of immuno-organoid co-cultures from each condition were harvested 5, 24 and 48 h post treatment. At 4 h preceding culture harvest at each time point, wells were treated with Protein Transport Inhibitor Cocktail (ThermoFisher) to facilitate intracellular accumulation of cytokine protein. Co-cultures were washed with PBS and then digested to single cells using Accutase solution (STEMCELL Technologies) at room temperature for approximately 30 min. Cell suspensions were passed through a 70 µm strainer and stained for surface proteins (Supplementary Table 3). Cells were then fixed and permeabilized using the Foxp3 Transcription Factor Staining Buffer Set (ThermoFisher), and subsequently stained for intracellular and intranuclear proteins. Stained cell suspensions were acquired on a BD Fortessa X-20 using BD FACSDiva Software v.9.7 and analysed using FlowJo v.10. Example gating strategies are shown within the source data of the relevant figures in Supplementary Information. To facilitate visual representation across one plot, samples from different time points and treatments were concatenated and separated along the *y* axis.

Luminex supernatant analysis of immune-organoids

Following sampling, supernatants were immediately stored at −80 °C until measurement. For measurement of cytokines (Gzmb, IFNγ, IL-2, IL-4, IL-6, IL-10, TNF, MCP-1, IP-10 and GM-CSF) the customized Invitrogen ProcartaPlex multiplex immunoassay (reference no. PPX-10-MXFVMZC) was applied and used according to the manufacturer's instructions. In short, capture beads were added to a 96-well flat-bottom plate, washed with an automatic plate washer (405TS microplate washer, Bioteck) and incubated with either the diluted supernatants or provided standards for 2 h at room temperature. Next the beads were washed and detection antibodies added to the plate for 30 min at room temperature, followed by a further wash step. The beads were

then incubated with Streptavidin-PE for a further 30 min at room temperature before final washes. Lastly the beads were resuspended in the acquisition buffer and the plate was read on a Bio-Plex-200 instrument (Bio-Rad) using the corresponding Bio-Plex Manager Software v.6.2.

Isolation of T cell subsets for organoid co-culture

For organoid co-culture with specific subsets of immune cells, magnetic-activated cell separation MS columns and MicroBeads (Miltenyi Biotec) were used for subset enrichment following the manufacturer's instructions. To enrich memory T cells from PBMCs, CD45RO MicroBeads were used (Miltenyi Biotec). To enrich for $CD103^{+/-}$ cells from T_{RM} cells, cells were first labelled with biotin anti-human CD103 antibody (BioLegend) and subsequently purified using anti-biotin MicroBeads (Miltenyi Biotec). Purity of the enriched cells was validated by flow cytometry.

Caspase 3/7-based epithelial cell cytotoxicity assay

Intestinal immuno-organoid cultures were prepared in 4 µl of Matrigel Matrix GF per well of a PhenoPlate 96-well microplate (Revvity), with cell ratios and media as described above. Apoptosis was assessed using the CellEvent Caspase 3/7 Detection Reagent (Invitrogen), either during TCB treatment or at specific intervals. CellEvent Caspase 3/7 Detection Reagent was added to culture medium at 1:1,000. Samples were imaged in confocal mode at ×5 magnification (air objective) with an Operetta CLS (Perkin Elmer) covering approximately a 450 µm z-stack, starting at −150 µm. Distance between z-stacks was set to the minimum of 27 µm for the ×5 objective (autofocus, two-peak; binning, 2). Channels selected were bright-field and predefined AlexaFluor 488. Per well, five fields were acquired, covering nearly the entire surface of the 96-well PhenoPlate plate; CO_2 was set to 5% and temperature to 37 °C. Caspase 3/7 fluorescence signal intensity was quantified using Opera Harmony software v.4.9 (PerkinElmer). Briefly, segmentation of organoids was done using 'Find Texture Regions' based on the bright-field signal only, followed by 'Select Region' and 'Find Image Region' to segment single organoids as objects. Next, 'Calculate Morphology Parameters' was performed to select objects above 10,000 μm^2 with 'Select Population'. Next, Caspase 3/7 fluorescence signal per individual organoid was determined using 'Calculate Intensity Properties' of the AF 488 channel within these objects.

Time-lapse imaging of IIOs

Before IIO or organoid + PBMC-derived T cell co-culture, matched T_{RM} cells and PBMCs were thawed and apoptotic cells removed using the Dead Cell Removal Kit (Miltenyi Biotec). T cells were isolated from PBMCs using the EasySep Human T Cell Isolation Kit (no. 17951, STEMCELL Technologies) and the EasySep Magnet (no. 18000, STEMCELL Technologies), following the manufacturer's instructions. Immune cells were labelled with CellTrace Far Red (no. C34564, ThermoFisher) and IIO or PBMC + organoid co-cultures were prepared as described in 'Preparation and culture of intestinal immune-organoids, including treatment'. Time-lapse live imaging was performed 16 h post co-culture set-up with a Leica STELLARIS 8 confocal microscope using a water-immersion objective (HC FLUOTAR L VISIR ×25/0.95 numerical aperture WATER) and 0.85 zoom. Images were obtained in bidirectional mode with 1,024 × 1,024 pixels at 600 Hz. Images were acquired every 38 s with 84 µm z-stacks (z-steps, 4 µm). Samples were imaged between 42 and 60 min, where indicated. During imaging, samples were maintained in an incubation chamber (The Box, Life Imaging Services) at 37 °C and 5% CO_2. Following acquisition, maximum-intensity projections were generated with Leica Las X software and later exported as AVI files using ImageJ v.1.54i. Cell videos were analysed using CellProfiler v.4.2.5. The number of frames per condition was equalized for direct comparison. Briefly, cells were segmented at each frame with Multi-Otsu, morphological parameters were extracted and segmented cells were tracked over time using an overlap of two pixels. The output per cell was analysed using KNIME v.5.2.4. The means and standard deviation of morphological features per track over time were calculated. The standard deviation of morphological features over time is a measure of the dynamism of cells because they use amoeboid motility. In addition, track lifetime and track total distance were calculated. Tracks with fewer than 20 frames were discarded.

Monocyte-derived dendritic cell generation for ICI experiments

Monocyte-derived dendritic cells were generated using the Mo-DC generation Toolbox (Miltenyi Biotec) following the manufacturer's instructions. Briefly, monocytes were isolated from PBMCs by magnetic separation over magnetic-activated cell separation columns with CD14 MicroBeads. Monocytes were cultured in standard tissue culture flasks in the provided Mo-DC Differentiation Medium for 7 days, with renewal of the medium every 2–3 days. Maturation of dendritic cells was initiated at day 7 for 3 days by the addition of 6,000 IU ml^{-1} human TNF (Miltenyi Biotec). One day before usage, 100 ng ml^{-1} lipopolysaccharide (Sigma-Aldrich) was added to activate dendritic cells overnight. Cells were harvested by incubation in 2× EDTA in PBS for 10 min at 37 °C. Dendritic cells were counted and plated at 40,000 per well of an ultralow-attachment, round-bottom, 96-well plate (Corning). T_{RM} cells and PBMCs from the same donors were thawed, counted and combined with dendritic cells at 120,000 cells per well. Either immune checkpoint inhibitors (nivolumab and ipilimumab, both Bristol-Myers Squibb) or isotype controls were added at 20 µg ml^{-1}, in RPMI 1640 with 10% FCS. Dendritic/T cell co-cultures with or without ICIs were cultured for 4 days before combining immune cells with matched organoids. Organoids were harvested as described in the preparation and culture of IIO before being mixed with the corresponding cells from the mixed lymphocyte reaction. IIO cultures were plated in 5 µl of Matrigel Matrix GFR domes and maintained in 50:50 RPMI 1640 with 10% FCS (ThermoFisher) and IntestiCult Organoid Growth Medium (STEMCELL Technologies) for 48 h, with or without ICIs. Cell death was monitored by live imaging with Caspase 3/7, and LDH in the supernatant was measured every 24 h.

LDH assay

Supernatants of the triculture were used directly following sampling for measurement. A cytotoxicity detection kit (Roche) was used according to the manufacturer's instructions. Briefly, the standard curve was prepared and supernatants were diluted in PBS and incubated with the reaction mix for 30 min at room temperature in the dark. Following incubation the plate was read using a PerkinElmer Envision 2104 Multilable reader with absorbance at 490 nm.

Recombinant TNF treatment of organoid cultures

Four days following passage, organoids were harvested with cell recovery solution (Corning) and seeded onto a PhenoPlate 96-well microplate (Revvity) in 5 µl of Matrigel Matrix GFR droplets. Organoids were treated for 72 h with human recombinant TNF (Miltenyi Biotec; highest dose, 156 ng ml^{-1}, seven-dose titration, fivefold dilution). TNF-induced apoptosis was monitored by live imaging every 2 h on an Operetta using the cell event Caspase 3/7 detection reagent as described above.

FFPE embedding of co-cultures

To formalin-fixed, paraffin-embedded (FFPE) co-cultures the samples were seeded in a 50% (v/v) Matrigel–Collagen I matrix. Wells were washed once with 1× DPBS before fixation with 4% paraformaldehyde (PFA) in the 24-well Clear TC-treated plate. Following 30 min of fixation at room temperature, the wells were washed three more times before complete aspiration of 1× DPBS; 400 µl of preliquefied HistoGel (ThermoScientific) was then dispensed into 24-well Clear TC-treated plates. Following polymerization of HistoGel (10 min at 4 °C), the organoid–HistoGel 'platelet' was carefully lifted out of the 24-well Clear TC-treated plate using a thin metallic spatula. Samples were then distributed into biopsy cassettes and dehydrated overnight

using a Vacuum filter processor (Sakura, TissueTek VIP5). The following day, samples were embedded in liquid paraffin.

Microtome sectioning

FFPE blocks were, in general, sectioned at a thickness of 5 µm and transferred on Superfrost Plus Adhesion microscope slides (Epredia). Where indicated, thickness differs. Slides were incubated in a slide oven overnight at 37 °C.

FFPE-based mIF

Multiplex immunofluorescence (mIF) staining of FFPE slides was performed using a Ventana Discovery Ultra automated tissue stainer (Roche Tissue Diagnostics). Slides were first baked at 60 °C for 8 min and subsequently further heated to 69 °C for 8 min for subsequent deparaffinization. This cycle was repeated twice. Heat-induced antigen retrieval was performed with Tris-EDTA buffer pH 7.8 (Ventana) at 92 °C for 32 min. After each blocking step with Discovery Inhibitor (Ventana) for 16 min, the Discovery Inhibitor was neutralized. Primary antibodies were diluted in Discovery Ab diluent (Ventana). Primaries were detected using appropriate anti-species secondary antibodies conjugated to horseradish peroxidase (HRP, OmniMap Ventana; Supplementary Table 3). Subsequently, the relevant Opal dye (Akoya Biosciences) was applied. Following every application of a primary, respective secondary antibody and Opal dye, an antibody neutralization and HRP-denaturation step was applied to remove residual antibodies and HRP before starting the staining cycle again with the Discovery Inhibitor blocking step. Lastly, samples were counterstained with DAPI (Roche).

mIF staining using Opal dyes from Akoya was digitized with multispectral imaging by Vectra Polari (PerkinElmer) using MOTiF technology at ×20 magnification for all seven colours (Opal 480, Opal 520, Opal 570, Opal 620, Opal 690, Opal 780 and DAPI). Slides were scanned in a batch manner to ensure identical imaging settings and cross-comparability for subsequent image analysis with HALO AI. Next, unmixing of channels and tiling of images was performed with PhenoChart (v.1.0.12) and inForm (v.2.4). Tiles were fused in HALO (Indica labs, v.3.2.1851.328).

High-resolution mIF was obtained using a STELLARIS 8 microscope (Leica) with a ×40/1.1 numerical aperture water-immersion objective (HC FLUOTAR L VISIR ×25/0.95 numerical aperture WATER) and 1.0 zoom. A white-light laser (440–790 nm) facilitated imaging of all Opal dyes mentioned above, and channels were acquired sequentially to reduce cross-talk. Images were obtained in bidirectional mode with 2,048 × 2,048 pixels (pixel size, 273.8 × 273.83 nm^2) at 600 Hz. Where indicated, images were acquired with z-stacks of 10–15 µm (z-steps, 1 µm), three-dimensionally reconstructed and shown in 'Maximum' mode using Leica Application Suite X software (Leica).

Image analysis by FFPE-based mIF

Image analysis of mIF images was performed with HALO AI (Indica Labs, v.3.2.1851.328). Briefly, single organoids were automatically detected using a deep learning algorithm trained to distinguish matrix and organoids (iterations, 5,000; cross-entropy, 0.32; DenseNet AI V2 Plugin). Following rapid validation, organoids were annotated as individual regions of interest, objects. Only objects over 7,500 $µm^2$ were considered positive.

The HighPlex FL v.4.2.14 module was used to perform nuclear segmentation based on $DAPI^+$ cells (assisted by HALO's integrated AI-default 'nuclear segmentation type') and specific marker identification. For quantification, $DAPI^+$ nuclei and markers for each distinct cell type of interest were merged (taking membranous and nuclear signals into account). Either secondary-only negative controls on the tissue of origin or organoid samples embedded within the same block served, and were then exposed to the full antibody-staining panel as a negative control sample to set the threshold for prevention of biased adjustments. The HighPlex FL analysis module was deployed on previously generated regions of interest of the organoids using integration of the classifier in the module. The number of T cells integrated/infiltrated into the organoid was normalized according to either the number of epithelial cells (non-TCB-treated organoids) or organoid area (EpCAM-targeted organoids). Surface markers of distinct T cells were used to phenotype these accordingly. Data was exported from HALO and analysed in GraphPad prism.

Single-cell dissociation of IIOs

Intestinal immuno-organoids were dissociated as described previously[62]. In short, organoids were dislodged, mechanically dismantled and transferred to 1% BSA-coated tubes. Organoid fragments were centrifuged at 400*g* for 4 min at room temperature. The supernatant was removed and enzymes of the neural tissue dissociation kit (Miltenyi Biotec) were mixed in HBSS/1%BSA buffer. Organoid fragments were then dissociated to single cells for a total of 30 min with thorough pipetting every 7 min. Next, cells were filtered through a 40 µm filter, with single cells centrifuged at 450*g* for 4 min at room temperature and subsequently resuspended in DPBS 1% BSA. Single-cell libraries were prepared on the 10X Genomics platform using the Chromium Next GEM Single Cell 3' Kit v.3.1.

scRNA-seq data preprocessing

CellRanger (v.6.0.2, 10X Genomics) was used to extract unique molecular identifiers, cell barcodes and genomic reads from the sequencing results of 10X Chromium experiments. Next, count matrices, including both protein coding and non-coding transcripts, were constructed aligning against the annotated human reference genome (GRCh38, v.3.0.0, 10X Genomics). For removal of potentially damaged or unhealthy cells and improvement in data quality, the following filtering steps were performed in addition to the built-in CellRanger filtering pipeline. Cells associated with over 50,000 transcripts—usually less than 1% of the total number of samples—were removed; and cells associated with a low number of unique transcripts—fewer than 500 unique transcripts detected (1% of the total number of samples)—were removed. Cells with over 20% of mitochondrial transcripts were removed. Transcripts mapping to ribosomal protein coding genes, as well as to mitochondrial genes, were removed, together with transcripts detected in fewer than ten samples.

Normalization with SCTransform

For normalization and variance stabilization of the molecular count data of each scRNA-seq experiment we used the modelling framework of SCTransform in Seurat v.3 (ref. 63). In brief, a model of technical noise in scRNA-seq data is computed using 'generalized gamma poisson regression'[64]. The residuals for this model are normalized values that indicate divergence from the expected number of observed unique molecular identifiers (UMIs) for a gene in a cell, given that gene's average expression in the population and cellular sequencing depth. In addition, a curated list of cell cycle-associated genes, available within Seurat, was used to estimate the contribution of cell cycle and remove this source of biological variation from each dataset to increase the signal deriving from more interesting processes. The residuals for the top 2,000 variable genes were used directly as input for computation of the top 100 principal components by principal component analysis (PCA) dimensionality reduction through the RunPCA() function in Seurat. Corrected UMIs, which are converted from Pearson residuals and represent expected counts if all cells are sequenced at the same depth, were log transformed and used for visualization and differential expression analysis.

Both primary intestinal biopsy samples and primary multiorgan biopsy samples were processed as described above. However, these did not undergo any cell filtering because quality control steps had already been performed in the respective published studies.

Doublet removal with DoubletFinder

For each scRNA-seq experiment, DoubletFinder[65] (v.2.3.0) was used to predict doublets in the sequencing data. In brief, this tool generates artificial doublets from existing scRNA-seq data by merging randomly selected cells, which are then preprocessed together with real data and jointly embedded on a PCA space that serves as a basis for finding each cell's proportion of artificial *k*-nearest neighbours. For this step we restricted the dimension space to the top 50 principal components. Finally, the proportions of artificial *k*-nearest neighbours values were rank ordered according to the expected number of doublets, and optimal cut-off selected through receiving operating characteristic analysis across p*N*–p*K* parameter sweeps for each scRNA-seq dataset: p*N* describes the proportion of generated artificial doublets, with p*K* defining principal component neighbourhood size. To achieve maximal doublet prediction accuracy the mean variance-normalized bimodality coefficient was leveraged. This provides a ground-truth-agnostic metric that coincides with p*K* values that maximize area under the curve in the data. To overcome DoubletFinder's limited sensitivity to homotypic doublets, we consider doublet number estimates based on Poisson statistics with homotypic doublet proportion adjustment assuming 1/50,000 doublet formation rate of the 10X Chromium droplet microfluidic cell loading.

Ambient messenger RNA signal removal

Following doublet prediction and removal we analysed each scRNA-seq dataset to estimate the extent of ambient mRNA contamination in every single cell and correct it. We used the R package Cellular Latent Dirichlet Allocation (CELDA)[66] (v.1.16.1), which contains DecontX and is a method based on the Bayesian statistical framework used to computationally estimate and remove RNA contamination in individual cells without empty droplet information. We applied the DecontX() function in CELDA to the raw count matrices with default parameters. Subsequently, we removed all cells with contamination values above 0.5 and used the decontaminated count matrices resulting from DecontX() for downstream analysis.

Geometric sketching

Geometric sketching is a downsampling technique that helps explore and interpret scRNA-seq data more effectively by providing a concise and intuitive representation of the cellular landscape that preserves rare populations. We used the sketchData() function from CellChat[67], with default parameters, to select one-third of the sequenced cells for each donor in the homeostatic samples described in Extended Data Fig. 2 (scRNA-seq samples for donor no. 1–3). This strategy was used to avoid variability in sequence efficiencies that influence the computation of lower-dimensional embeddings and heterogeneity analysis.

Data integration

Individual datasets—following preprocessing, doublet removal and ambient mRNA regression—were aggregated according to specific criteria (for example, tissue of origin, profiling time, culture condition) and underwent a joint normalization step with SCTransform to mitigate technical confounding factors, which also served as a means for selection of a meaningful set of the 2,000 most variable global genes before data integration. Integration of different conditions (culture model, treatment and time points) was performed using the log-normalized, corrected UMI count data in two steps. First, the residuals for the top 2,000 global variable genes were used as input in computing the top 100 principal components through the RunPCA() function in Seurat. The 30 leading principal components and 50 nearest neighbours were then used to define the shared neighbourhood graph with the FindNeighbors() function in Seurat. Subsequently, datasets were clustered according to the shared neighbourhood graph using the Louvain algorithm[68] through the Seurat function FindClusters(), with resolution 0.8. Finally, we used these high-resolution clusters to define a restricted, noise-reduced and cell state-specific set of genes ('Differential expression analysis'). In the second step of the integration process we compiled a list consisting of the ensemble of the 30 top differentially expressed genes for each cluster and used it to focus and repeat PCA dimensionality reduction. The first 30 principal component vectors of the new PCA space served as the basis for obtaining a two-dimensional representation of the data through UMAP[69] implemented in RunUMAP() with the 50 nearest neighbours. We then computed a shared neighbourhood graph on the UMAP lower-dimensional space and computed the final integrated clusters with resolution parameter 0.2.

Integration index

The integration index of T cells in the homeostatic samples described in Fig. 2 and Extended Data Fig. 2 was computed by identification of the 50 closest neighbours of each T cell on the lower-dimensional space defined by the 30 leading CCA vectors. Subsequently, the proportion of PBMC-derived T cell neighbours was subtracted from the proportion of IIO-derived T cell neighbours of each individual cell and the resulting index was mapped to an interval of 0–1.

Differential expression analysis

Gene differential expression analysis between distinct cell populations in scRNA-seq data was assessed by performing Wilcoxon rank-sum tests and area under the receiving operating characteristic analysis, as implemented by the Presto (v.1.0.0) package in R. log-transformed, corrected UMIs were used as input for differential expression statistical tests, and genes were called differentially expressed if the associated adjusted *P* value (Bonferroni method) was lower than 0.05, area under the curve value above 0.6 and log fold change greater than 0.15. In addition, we also set thresholds on detection rates of differential expression genes. In particular, a given gene was assigned as overexpressed in the analysed group if it was detected in at least 30% of the samples of that group, whereas detection rate in background samples was at most 70% of the detection rate of the analysed group.

$CD8^+$ T cell activation trajectory reconstruction

For reconstruction of the continuum of the $CD8^+$ T cell activation trajectory in IIO models challenged with bispecific antibodies, we took advantage of diffusion pseudotime as implemented in the destiny package (v.3.14.0) in R. In brief, diffusion pseudotime uses random-walk-based distance, computed on the leading eigenvectors of a transition matrix, to order scRNA-seq data according to differentiation stages[44,70]. We used the DiffusionMap() function in the destiny package on the space identified by the 30 leading principal component vectors of the integrated PCA embedding of $CD8^+$ clusters. Pseudotime values were then computed with the DTP() function in destiny on the diffusion map object using default parameters. Similarly global pseudotime, following *TNF* perturbation simulation, was based on a random-walk approach on the cell-state transition matrix.

Intercellular communication analysis

For investigation of ligand–receptor-mediated cell–cell communication during immune cell activation in our IIO models we focused on the signals exchanged between T_H1 cells, activated T-bet B cells and $CD8^+$ CTLs. For this analysis we extracted genes labelled as either ligands or receptors from curated databases[53] and required that these genes be differentially expressed between the three populations under investigation, which facilitated retrieval of directional information about signal exchange. To gain insights into functional cell–cell communication we used the NicheNet (v.02.01.2000) pipeline, which considers the influence of sender-cell ligands on receiver-cell gene expression[53]. NicheNet's analysis pipeline provided us with a ranking of predicted ligands that most probably affect gene expression in activated

T-bet B cells and $CD8^+$ CTLs, highlighting the role of critical T_H1-secreted factors in driving immune cell phenotypes within IIOs.

Functional enrichment analysis

To gain an understanding of the mechanisms underlying phenotypes in our data, differentially expressed genes were analysed for Gene Ontology biological process enrichment using one-sided hypergeometric testing. *P* values were adjusted for multiple testing hypotheses by the Bonferroni method, and only those enrichment results below a 5% significance level threshold were considered. For this analysis we considered only those biological processes consisting of sets with more than 10 but fewer than 300 mapped genes.

In silico perturbation analysis

To simulate dynamic shifts in cell identity resulting from ligand signalling cascade activation we used Nichenet's prior model[53]. The first step involved the generation of simulated values by applying the gene regulatory network as a function and propagating the relative changes in gene expression following *k*-nearest-neighbour imputation of the gene expression data. This iterative (three times) signal propagation enabled us to calculate the broad, downstream effects of ligand perturbation, thereby estimating the global transcriptional shift. The estimation of cell-identity transition probability was accomplished by comparing this gene expression shift with that of local neighbours, utilizing a likelihood-based dynamical model. By doing so we could establish a measure of how cell identities transition in response to ligand perturbation. Finally, the transition probabilities were transformed into a weighted local average vector map, encoding the simulated directionality of cell-state transition for each cell. This workflow results from an adaptation and integration of CellOracle[71] and scVelo[72] in Python (v.3.7).

Reporting summary

Further information on research design is available in the Nature Portfolio Reporting Summary linked to this article.

Data availability

Sequencing files in FASTQ format supporting single-cell transcriptomic analysis of homeostasis conditions, as well as EpCAM TCB treatment, have been deposited in ArrayExpress and are accessible at E-MTAB-14171 and E-MTAB-14170, respectively. Raw count matrices, together with metadata information, for all scRNA-seq samples discussed in this study have been deposited in Mendeley and are available at https://data.mendeley.com/datasets/5h3ym82bnb/1. Source data underlying all graphical representations used in the figures are provided as Supplementary Information. Source data are provided with this paper.

62. Yu, Q. et al. Charting human development using a multi-endodermal organ atlas and organoid models. *Cell* **184**, 3281–3298 (2021).
63. Hafemeister, C. & Satija, R. Normalization and variance stabilization of single-cell RNA-seq data using regularized negative binomial regression. *Genome Biol.* **20**, 296 (2019).
64. Ahlmann-Eltze, C. & Huber, W. glmGamPoi: fitting gamma-Poisson generalized linear models on single cell count data. *Bioinformatics* **36**, 5701–5702 (2021).
65. McGinnis, C. S., Murrow, L. M. & Gartner, Z. J. DoubletFinder: doublet detection in single-cell RNA sequencing data using artificial nearest neighbors. *Cell Syst.* **8**, 329–337 (2019).
66. Wang, Z. et al. Celda: a Bayesian model to perform co-clustering of genes into modules and cells into subpopulations using single-cell RNA-seq data. *NAR Genom. Bioinform.* **4**, lqac066 (2022).
67. Jin, S. et al. Inference and analysis of cell-cell communication using CellChat. *Nat. Commun.* **12**, 1088 (2021).
68. Blondel, V., Guillaume, J., Lambiotte, R. & Lefebvre, E. Fast unfolding of communities in large networks. *J. Stat. Mech.* https://doi.org/10.1088/1742-5468/2008/10/P10008 (2008).
69. McInnes, L., Healy, J., Saul, N. & Großberger, L. Uniform manifold approximation and projection. *J. Open Source Softw.* **3**, 861 (2018).
70. Coifman, R. R. et al. Geometric diffusions as a tool for harmonic analysis and structure definition of data: diffusion maps. *Proc. Natl Acad. Sci. USA* **102**, 7426–7431 (2005).
71. Kamimoto, K. et al. Dissecting cell identity via network inference and in silico gene perturbation. *Nature* **614**, 742–751 (2023).
72. Bergen, V., Lange, M., Peidli, S., Wolf, F. A. & Theis, F. J. Generalizing RNA velocity to transient cell states through dynamical modeling. *Nat. Biotechnol.* **38**, 1408–1414 (2020).

Acknowledgements We thank R. Sriram for supporting us with the establishment and oversight of the research agreements governing access to human intestinal specimens. We acknowledge the support of the non-profit foundation HTCR, which holds human tissue on trust, making it broadly available for research on an ethical and legal basis.

Author contributions T.R., N.G., J.G.C., L.C. and M. Bscheider conceived the study. T.R., N.G. and J.G.C. wrote the manuscript. T.R., L.S. and M.F.H. were involved in designing and performing most experiments in the manuscript. B.G. and L.A. led the bioinformatics efforts and analysed all scRNA-seq data. T.R., L.S., M. Bellavista, U.K. and D.P. performed scRNA-seq experiments. L.S., M.F.H., K.K., M.P.M. and G.L. performed revision experiments. M.N., R.K. and M. Bickle performed or analysed live-imaging experiments. T.R., L.S., R.G., M.P.M. and B.S. isolated and banked organoids and T_{RM} cells from primary intestinal samples.

Competing interests All authors are employees of Hoffmann-LaRoche. The company provided support in the form of salaries for authors but did not have any additional role in the study design, data collection and analysis, decision to publish or preparation of the manuscript.

Additional information
Supplementary information The online version contains supplementary material available at https://doi.org/10.1038/s41586-024-07791-5.

Correspondence and requests for materials should be addressed to Lauriane Cabon, J. Gray Camp or Nikolche Gjorevski.

Peer review information *Nature* thanks Linheng Li, Toshiro Sato and the other, anonymous, reviewer(s) for their contribution to the peer review of this work. Peer reviewer reports are available.

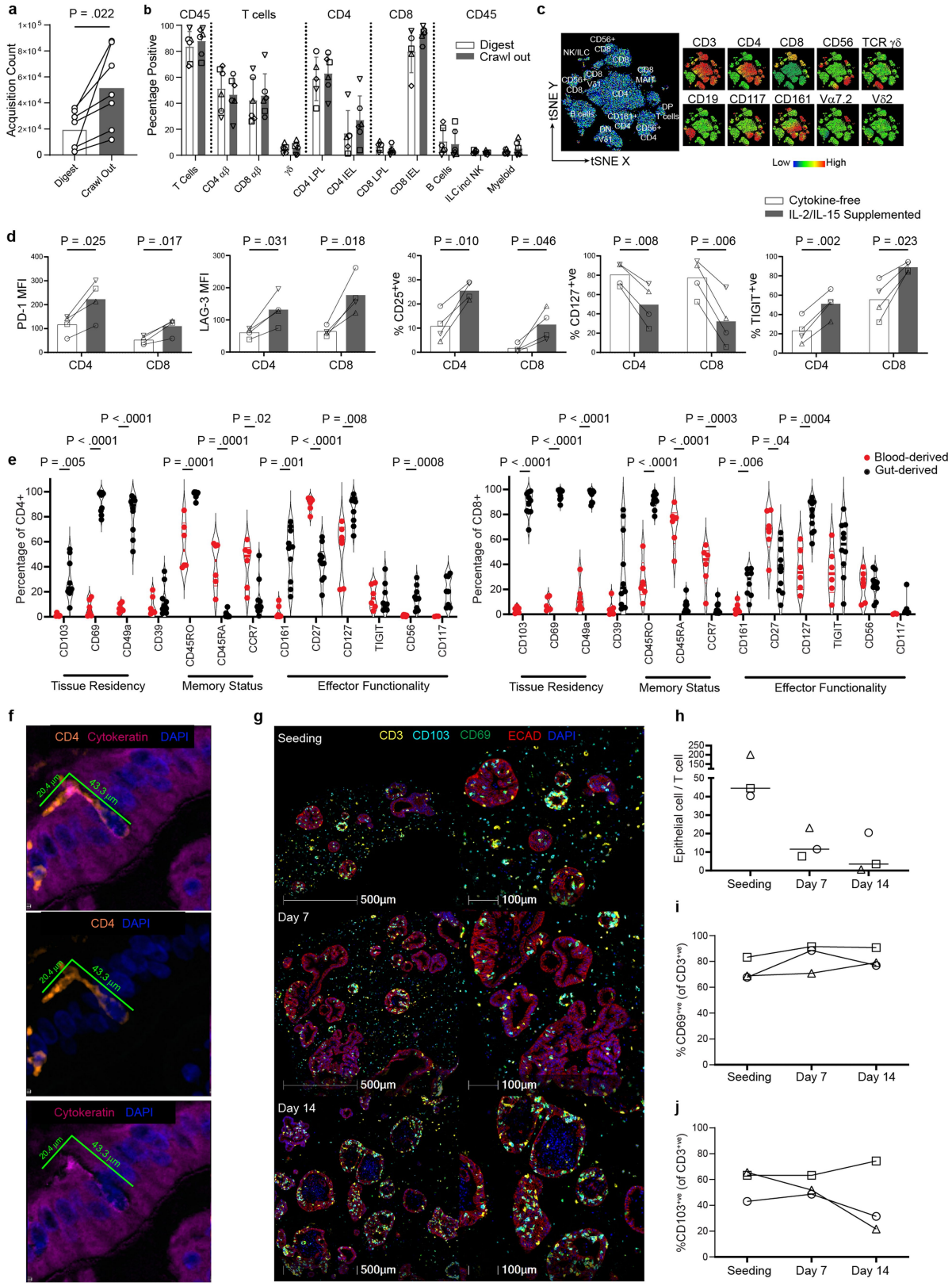

Extended Data Fig. 1 | See next page for caption.

Extended Data Fig. 1 | Intestinal TRM isolation and comparison to circulating T cells. a, Comparison of viable $CD45^+$ count in matched donors subjected to either digestion- or crawl out- based isolation. Two-tailed paired T-test. 7 biological replicates. **b**, Comparison of immune cell proportions subjected to either digestion- or crawl out- based isolation. Values represent percentages of parent population listed above each bar, as determined via flow cytometry. LPL lamina propria lymphocyte, IEL intraepithelial lymphocyte. Mean ± SD of 5 (Digest CD4 LPL, CD4 IEL, CD8 LPL, CD8 IEL, B cells) or 6 (all other conditions) biological replicates. Different symbol shapes represent individual donors. **c**, Flow cytometry-generated tSNE analysis of one intestinal lymphocyte isolation incorporating lineage-defining immune cell markers. Leftmost plot represents annotated cell populations with smaller plots displaying heatmaps for each of the 10 key surface markers assessed. DP double positive, DN double negative. Data is representative of six biologically-independent replicates. **d**, Bar charts comparing expression of key activation markers in gut-derived $CD4^+$ and $CD8^+$ T cells isolated via crawl out in cytokine-free or cytokine-supplemented (10IU/ml IL-2, 2 ng/ml IL-15) media in four biological replicates. Two-tailed paired T-test. **e**, Flow cytometry assessment of key functionality markers in $CD4^+$ T cells (left graph) and $CD8^+$ T cells (right graph) after crawl out isolation. Violin plots collate data from 10 (8 for CD117) independent intestinal tissue resections, 5 (3 for CD117) of which have matched blood-derived comparators, with 1 additional blood only sample. Two-tailed unpaired T-test between gut- and blood-derived expression values for each marker. **f**, mIF image of an elongated flossing T cell inserting itself between basal-lateral epithelial cell junctions. The 3 images are from the same region: upper image shows the full stain, middle image contains only CD4 and DAPI to emphasize the unusual shape of the T cell, lower image shows only DAPI and cytokeratin to reveal the space in the epithelium generated by the CD4 cell integration. Diameter of the T cell from head to tail is listed. Similar elongated T cells were observed in all IIO cultures analysed by mIF (n = 5). **g**, Representative mIF image of the IIO culture over time (upon immune cell introduction, 7 and 14 days later). Markers for T cell (CD3) and epithelial cell (ECAD: E-cadherin) identity, and tissue-residence (CD103 and CD69) are included. Data are quantified in (h-j). **h**, Ratio of epithelial cells to immune cells within identified organoids, during the course of a 14 day IIO culture. Line at median. **i-j**, Percent of $CD3^+$ T cells expressing CD69 (i) or CD103 (j) during the course of a 14 day IIO culture, as determined by mIF. Data from **h-j** is derived from 3 biological replicates, with each individual donor represented by a different symbol.

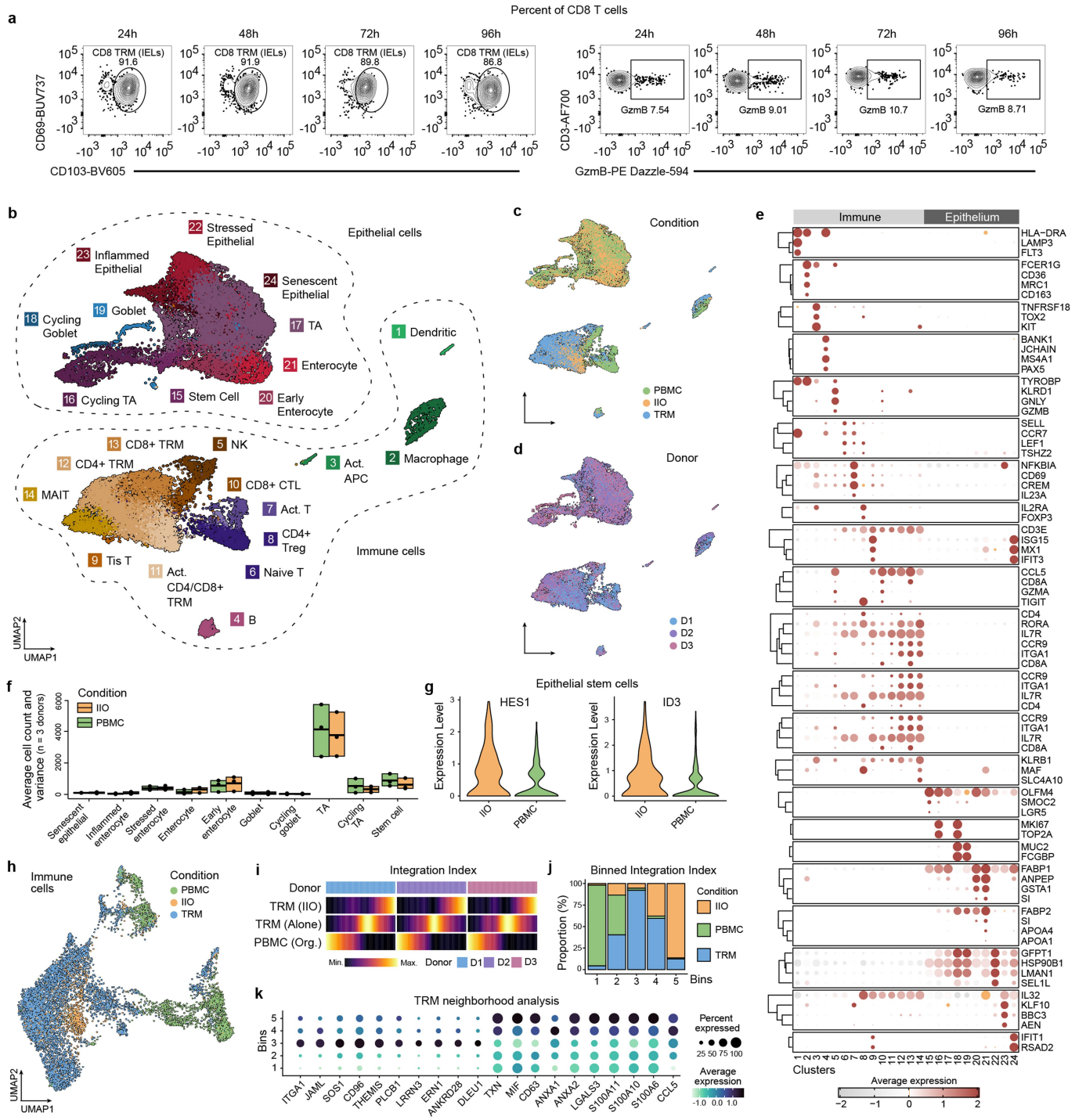

Extended Data Fig. 2 | Single-cell transcriptome analysis of homeostatic IIO model. a, Flow cytometry plots displaying daily CD8$^+$ TRM IEL proportions and GzmB expression in baseline (untreated) IIO cultures after digestion, across 96 h. Plots are representative of 3 independent IIO experiments. **b-d**, UMAP embeddings of single-cell transcriptome data colored by cell cluster (b), condition (c) and donor origin (d). The sequenced conditions include intestinal organoids containing TRMs (IIO), organoids containing PBMCs (PBMC) and TRMs cultured in matrigel (TRM). **e**, Dotplot summarizing marker gene expression across different immune (left) and epithelial (right) cell clusters. **f**, Boxplots displaying the minimum, mean and maximum number of cells across all donors (n = 3) for clusters of epithelial cells cultured with TRMs (IIO) or PBMCs (PBMC). **g**, Violin plots illustrating the expression of *HES1* and *ID3* transcription factors in intestinal epithelial stem cells cultured with TRMs or PBMCs. **h**, UMAP embedding of subsetted T cells colored by condition as portrayed in Fig. 2b. **i**, Heatmaps representing T cell densities along the reconstructed integration index vector for each condition (rows) and donor (groups) membership. **j**, Stacked barplot showing the proportion of TRMs cultured with epithelium (IIO), TRMs cultured in matrigel (TRM) and PBMCs cultured with epithelium (PBMC) within 5 equidistant bins of the integration index. **k**, Dotplot summarizing marker gene expression of TRMs cultured in matrigel (left, bin3) and TRMs cultured with epithelium (right, bin5).

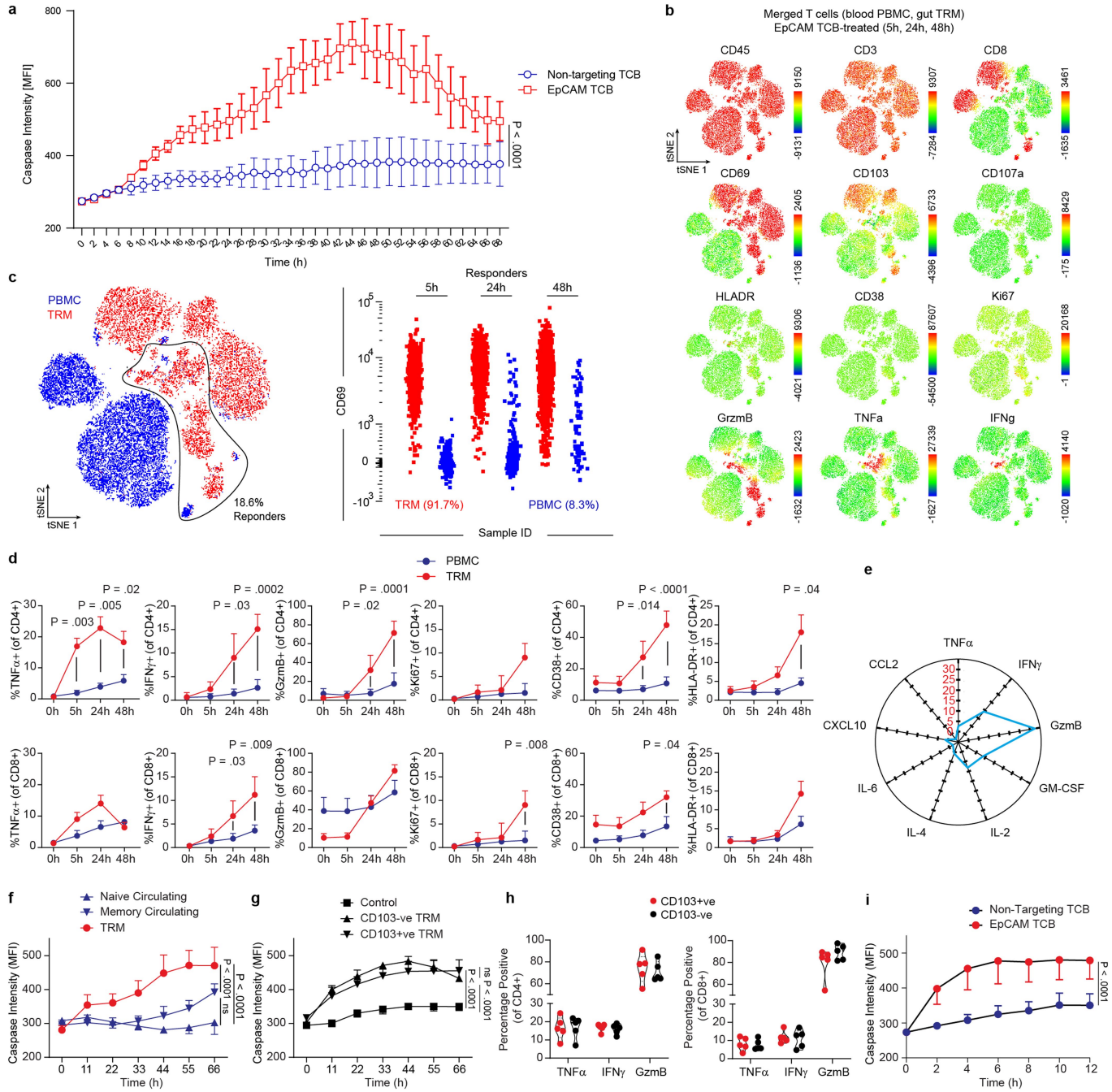

Extended Data Fig. 3 | See next page for caption.

Extended Data Fig. 3 | TRMs exhibit rapid and aggressive targeting of healthy epithelium following EpCAM-TCB treatment. a, Bihourly quantification of caspase 3/7 signal in IIO co-cultures for 68 h treated with either 5 ng/ml EpCAM TCB or a non-targeting control molecule, IIO triplicates representative of 3 independent biological replicates, mean ± SD. Two-tailed unpaired T-test of the area under the curve for each condition. **b**, Flow cytometry-generated tSNE analysis of all T cells at all timepoints, derived from one representative IIO co-culture and its matched PBMC-organoid co-culture control, treated with 5 ng/ml EpCAM TCB. Plots display heatmaps for each of the 12 surface and intracellular markers assessed by flow cytometry. **c**, Gating strategy for identifying responder cells (those that expressed TNF-α, IFNγ or GzmB), and the ungating of the concatenated flow cytometry files to reveal the original source of responder T cells. **d**, Expression of key soluble and cell surface factors in matched TRM and PBMC $CD4^+$ (top row) and $CD8^+$ (bottom row) T cells over 48 h, following IIO or matched PBMC-organoid co-culture treatment with 5 ng/ml EpCAM TCB, as determined via flow cytometry. Mean and SEM, 5 biological replicates (4 for Ki67). Statistically significant values between TRM and PBMC condition at each timepoint are displayed, 2-way ANOVA with Tukey's Multiple Comparisons Test. **e**, Cytokine fold-increase in IIO culture supernatants 48 h after 5 ng/mL EpCAM TCB treatment, relative to the matched PBMC-organoid co-culture control, as analysed via Luminex technology. Mean of 3 biological replicates. **f**, Quantification of caspase 3/7 signal in IIO co-cultures, versus matched organoid-PBMC co-cultures containing either circulating naive and memory T cells for 66 h treated with 5 ng/ml EpCAM TCB, culture quadruplicates representative of 3 independent biological replicates, mean and SD. One-way ANOVA of the area under the curve calculated for each condition. **g**, Quantification of caspase 3/7 signal in IIO co-cultures containing matched $CD103^+$ and $CD103^-$ TRMs for 66 h treated with 5 ng/ml EpCAM TCB or a non-targeting TCB, IIO quadruplicates (triplicates for CD103-ve TRM) representative of 3 independent biological replicates, mean and SD. One-way ANOVA of the area under the curve calculated for each condition. **h**, Flow cytometry assessment of TNF-α (24 h), IFNγ (48 h) or GzmB (48 h) in CD103+ and CD103- $CD4^+$ T cells (left graph) and $CD8^+$ T cells (right graph) from unsorted IIO cultures after treatment with 5 ng/ml EpCAM TCB. Violin plots collate data from 5 biological replicates. **i**, Quantification of caspase 3/7 signal in 10-day old IIO co-cultures treated with 5 ng/ml EpCAM TCB or a non-targeting TCB, IIO triplicates (non-targeting) or quadruplicates (EpCAM TCB) representative of 2 biological-independent replicates, mean and SD. Two-tailed unpaired T-test of the area under the curve calculated for each condition.

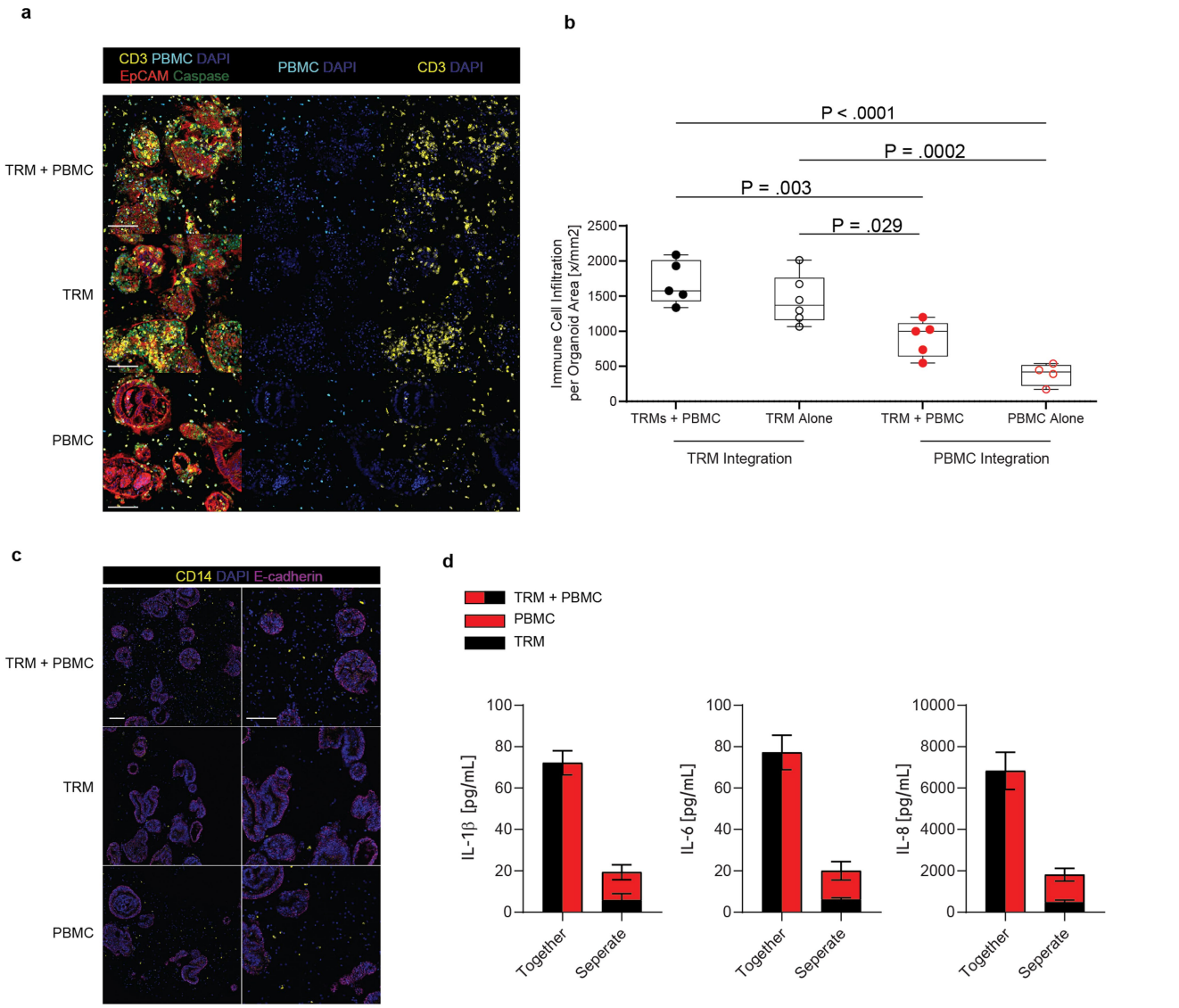

Extended Data Fig. 4 | TRM-generated inflammation promotes recruitment of circulating T cells into the epithelium. a, mIF images of TRM + PBMC (IIO + PBMC), TRM-alone (IIO) and PBMC-alone co-cultures with intestinal organoids, 18 h post treatment with 100 ng/ml EpCAM TCB treatment. EpCAM$^+$ organoids (red) surrounded by CD3$^+$ TRMs (yellow) and CellTracker CMFDA Green$^+$ CD3$^+$ PBMCs (cyan+yellow). Caspase 3 (green) captures TCB-triggered immune-induced apoptosis, nuclei are stained with DAPI (blue). Scale bar, 100 µm. Images are representative of four independent IIO experiments. **b**, Immune infiltration of TRMs, PBMC and TRMs+PBMC-organoid into organoids at 30 h post EpCAM TCB treatment. Data represented as boxplots, with whiskers showing all points (minimum to maximum) of the mean number of immune cells per individual organoid, summed and normalized to the sum organoid area for 4 (PBMC alone), 5 (TRM + PBMC) or 6 (TRM alone) independent IIO replicates. One-way ANOVA with Tukey's multiple comparisons test. **c**, mIF images of TRM + PBMC, TRM-alone and PBMC-alone co-cultures with intestinal organoids following 4 h treatment with 100 ng/ml EpCAM TCB. Monocytes (yellow) surround organoids (pink), nuclei are stained with DAPI (blue). Scale bar, 100 µm. Images are representative of four independent IIO experiments. **d**, Luminex quantification of IL-1β, IL-6 and IL-8 in the supernatants of the TRM + PBMC co-culture with organoids and the respective single immune cell condition, 30 h after treatment with 100 ng/ml EpCAM, 3 independent IIO replicates, representative of 3 biologically independent experiments. Mean and SD.

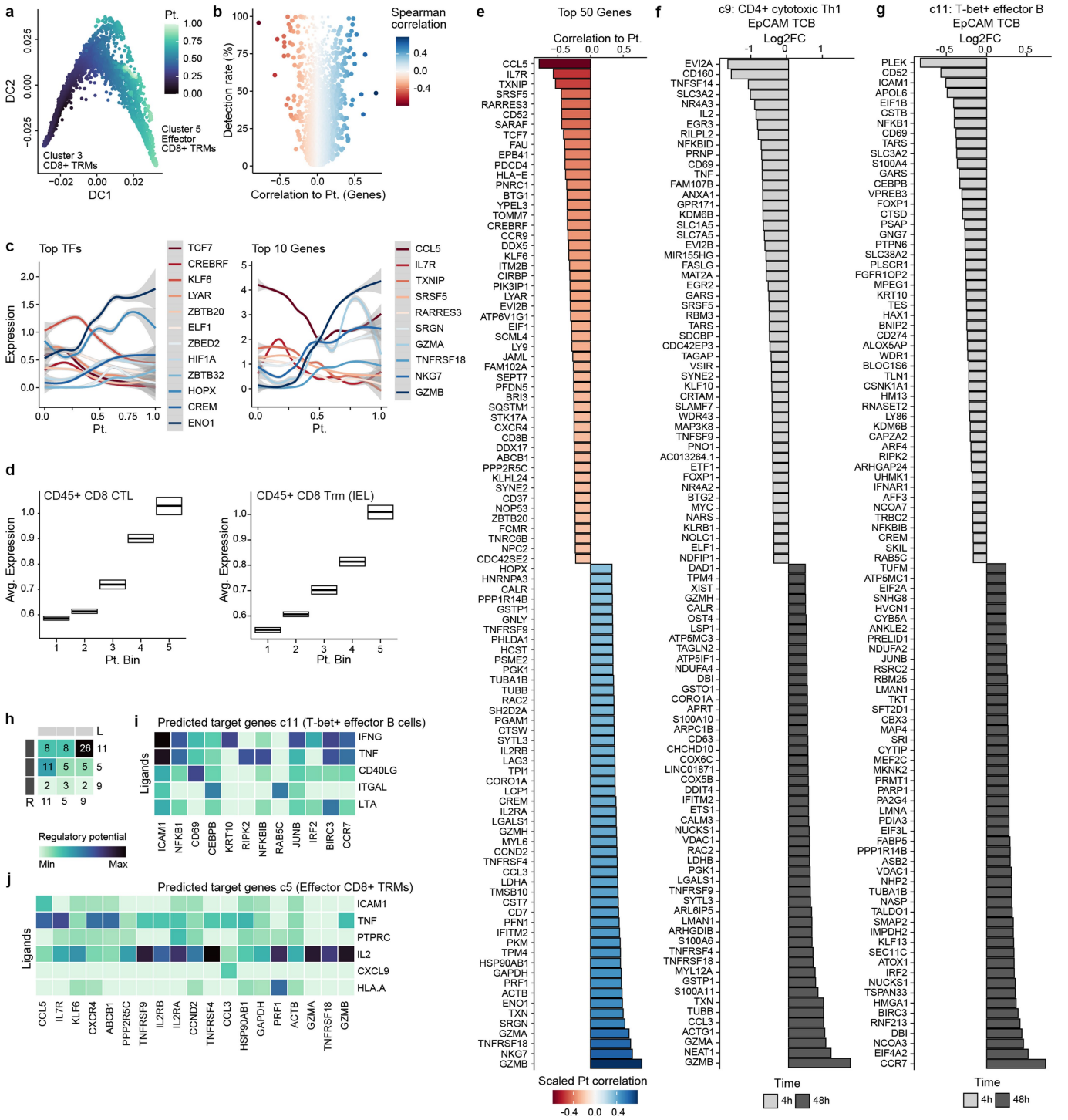

Extended Data Fig. 5 | Extended analysis of cell states and interactions in IIOs after treatment. a, Plot represents IIO CD8$^+$ T cells on the first two diffusion components colored by reconstructed diffusion pseudotime. **b**, Volcano plot showing variable genes along reconstructed CD8$^+$ T cell trajectory. x-axis represents spearman correlation value between gene expression and pseudotime value, y-axis represents detection rates of genes in the CD8$^+$ T cell populations. **c**, Expression patterns of most variable TFs (left) and effector genes (right) along the reconstructed CD8$^+$ T cell trajectory. **d**, Boxplot summarizing the expression pattern of CD8$^+$ CTL (left) and CD8$^+$ Trm IEL (right) gene signatures described in ref. 45 along the reconstructed activation trajectory of IIO CD8$^+$ T cells. x-axis represents 5 equidistant bins of the reconstructed pseudotime. Boxes represent the mean ± 95% CI computed from 100 bootstraps of the cells in each bin. **e-g**, Barplot showing differentially expressed genes in the CD8$^+$ T cell trajectory (e), in the CD4$^+$ cytotoxic Th1 population (c9) (f) and in the T-bet+ effector B cells (c11) (g) at 4 h and 48 h after EpCAM TCB treatment. **h**, Heatmap summarizes directed ligand-receptor pairing interactions of T-bet$^+$ effector B cells (c11) and T cell populations (clusters 5 and 9) in the IIO model. **i-j**, Predicted regulatory potential of CD4$^+$ cytotoxic Th1 cells (c9) ligands towards signature genes of T-bet+ effector B cells (c11) (i) and CD8$^+$ activated IELs (c5) (j).

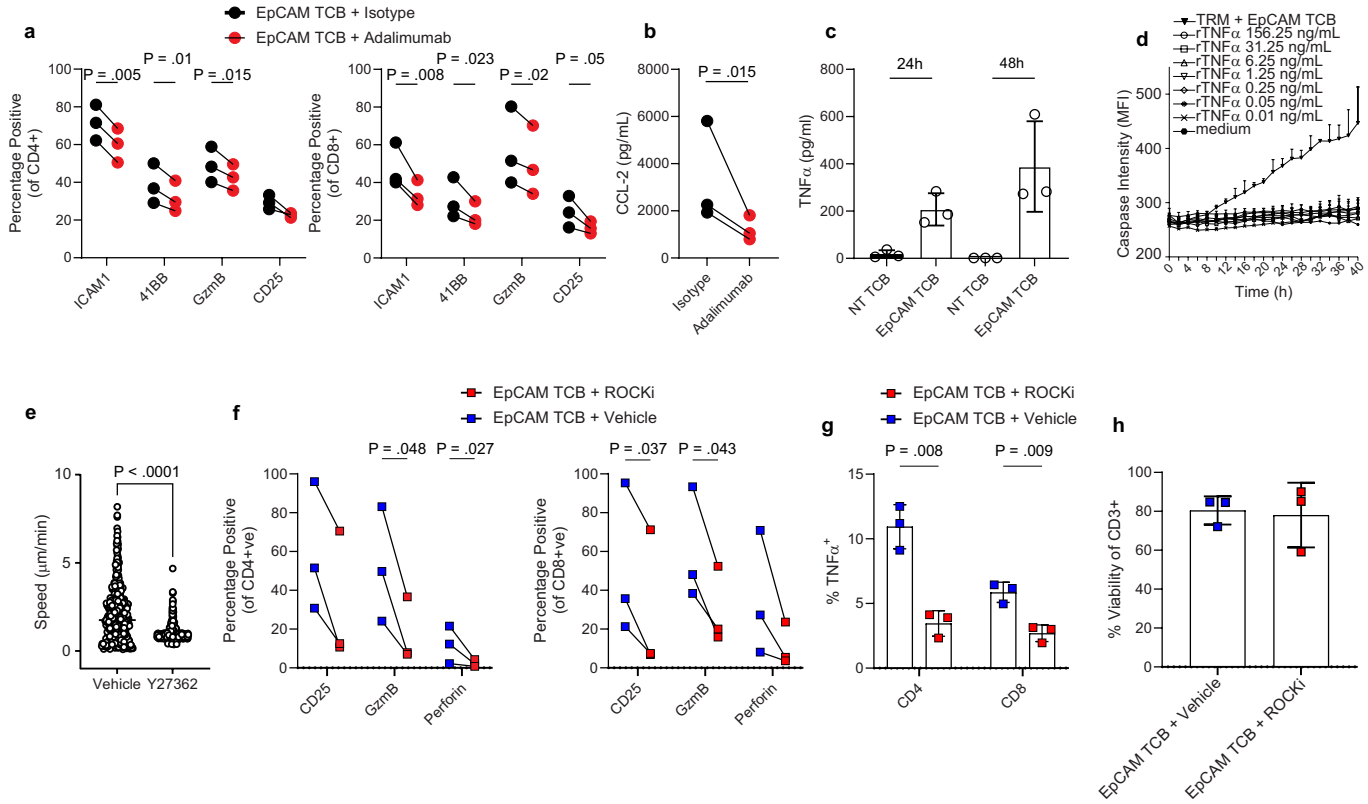

Extended Data Fig. 6 | Inhibition of TNF-α signaling and the ROCK1/2 pathway quells TRM-driven intestinal inflammation. a, Line graphs quantifying expression of predicted TNF-α targets associated with T cell activation and cytotoxicity, 48 h after treatment with 5 ng/ml EpCAM TCB in the presence of the TNF-α-neutralizing antibody Adalimumab or an isotype control. Left graph displays expression in $CD4^+$ T cells and the right graph displays expression in $CD8^+$ T cells. Two-tailed paired T-test. Data derived from three biological replicates. **b**, Luminex quantification of CCL2 chemokine in the supernatant of IIO cultures, 48 h after treatment with 5 ng/ml EpCAM TCB in the presence of the TNF-α-neutralizing antibody Adalimumab or an isotype control. Two-tailed paired T-test. Data derived from three biological replicates. **c**, Luminex quantification of TNF-α in the supernatants of IIO cultures, 24 h and 48 h after treatment with either 5 ng/ml EpCAM TCB or a non-targeting control. Data derived from three biological replicates. Mean and SD. **d**, Bihourly quantification of caspase 3/7 signal in organoid cultures treated with increasing concentrations of recombinant TNF-α cytokine for 40 h. TRM-containing IIO cultures treated with 5 ng/ml EpCAM TCB served as a positive control for caspase 3/7 induction. Technical triplicates representative of 2 independent biological replicates, mean and SD. **e**, CellProfiler assessment of TRM migration speed during 1 h live-imaging of IIO cultures, either in the presence of 10 μM ROCKi or vehicle control. Each dot represents a migrating cell tracked for more than 20 frames. Violin plots are a collation of duplicate videos from one IIO culture, n = 471 for vehicle and 546 for ROCKi treated. Similar results were observed in 3 biologically-independent IIO cultures. Bar shows mean. Two-tailed unpaired Mann-Whitney test. **f**, Line graphs quantifying expression of CD25, GzmB and perforin in $CD4^+$ T cells (left graph) $CD8^+$ T cells (right graph) isolated from IIO co-cultures 72 h after treatment with 5 ng/ml EpCAM-targeting T-cell bispecific antibodies in the presence of 10 μM ROCKi or vehicle control, as determined via flow cytometry. Two-tailed paired T-test, 3 biological replicates. **g**, Expression of intracellular TNF-α in $CD4^+$ T cells (left graph) $CD8^+$ T cells (right graph) isolated from IIO co-cultures 72 h after treatment with 5 ng/ml EpCAM-targeting T-cell bispecific antibodies in the presence of 10 μM ROCKi or vehicle control. Two-tailed paired T-test, 3 biological replicates, mean and SD **h**, Viability of T cells within IIO co-cultures 72 h after treatment with 5 ng/ml EpCAM-targeting T-cell bispecific antibodies in the presence of 10 μM ROCKi or vehicle control, as determined via flow cytometry. Cells were first gated based on CD3 expression and defined as viable via the live/dead dye Efluor780. n = 3 biological replicates, mean and SD.

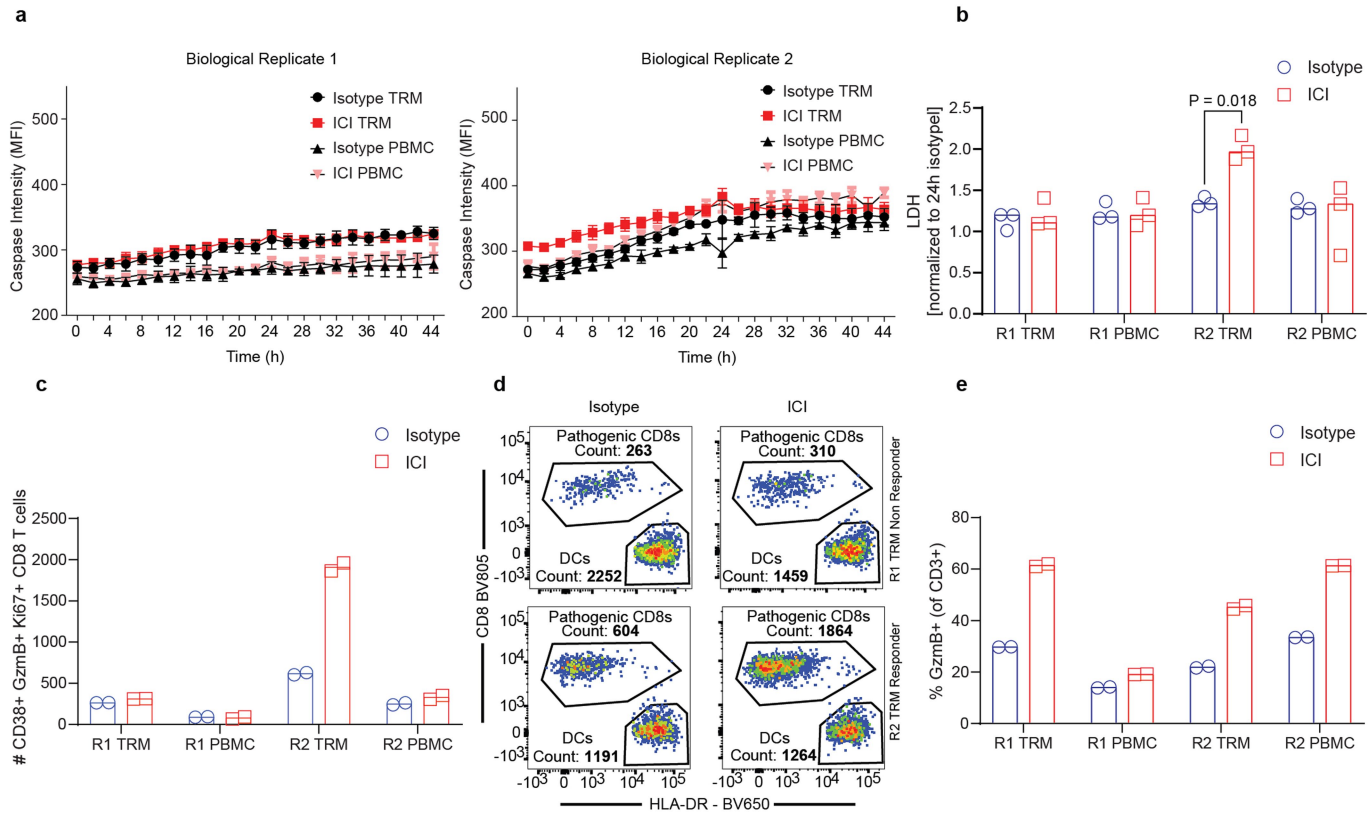

Extended Data Fig. 7 | IIO cultures provide a route to study ICI-induced colitis. **a**, Bihourly quantification of caspase 3/7 signal in ICI- or isotype- treated IIOs or matched PBMC-organoid co-cultures. 3-independent co-cultures from two biological replicates are shown. Mean and SD. **b**, LDH signal in the supernatant of the conditions described in **a** after 48 h of culture. Two-tailed paired T test. **c**, Flow cytometry quantification of the number of cytotoxic CD38$^+$ Ki67$^+$ GzmB$^+$ CD8$^+$ T cells within the conditions described in **a** after 48 h of culture. **d**, Boolean gating-derived flow cytometry plots showing the counts of CD38$^+$ GzmB$^+$ Ki67$^+$ "pathogenic" CD8$^+$ T cells and allogeneic DCs after 48 h of IIO culture in each of the TRM donors, treated with either an isotype control or ICI **e**, Flow cytometry quantification of the number GzmB$^+$ T cells within the conditions described in **a** after 48 h of IIO culture. ICI immune checkpoint inhibitor, R1 replicate 1, R2 replicate 2. DC dendritic cell.

nature portfolio

Corresponding author(s): Nikolche Gjorevski, Gray Camp, Lauriane Cabon

Last updated by author(s): Jun 3, 2024

Reporting Summary

Nature Portfolio wishes to improve the reproducibility of the work that we publish. This form provides structure for consistency and transparency in reporting. For further information on Nature Portfolio policies, see our Editorial Policies and the Editorial Policy Checklist.

Statistics

For all statistical analyses, confirm that the following items are present in the figure legend, table legend, main text, or Methods section.

n/a	Confirmed	
☐	☒	The exact sample size (*n*) for each experimental group/condition, given as a discrete number and unit of measurement
☐	☒	A statement on whether measurements were taken from distinct samples or whether the same sample was measured repeatedly
☐	☒	The statistical test(s) used AND whether they are one- or two-sided *Only common tests should be described solely by name; describe more complex techniques in the Methods section.*
☒	☐	A description of all covariates tested
☐	☒	A description of any assumptions or corrections, such as tests of normality and adjustment for multiple comparisons
☐	☒	A full description of the statistical parameters including central tendency (e.g. means) or other basic estimates (e.g. regression coefficient) AND variation (e.g. standard deviation) or associated estimates of uncertainty (e.g. confidence intervals)
☐	☒	For null hypothesis testing, the test statistic (e.g. *F*, *t*, *r*) with confidence intervals, effect sizes, degrees of freedom and *P* value noted *Give P values as exact values whenever suitable.*
☒	☐	For Bayesian analysis, information on the choice of priors and Markov chain Monte Carlo settings
☒	☐	For hierarchical and complex designs, identification of the appropriate level for tests and full reporting of outcomes
☒	☐	Estimates of effect sizes (e.g. Cohen's *d*, Pearson's *r*), indicating how they were calculated

Our web collection on statistics for biologists contains articles on many of the points above.

Software and code

Policy information about availability of computer code

Data collection	All sequencing data was enabled through 10X Chromium with initial collection and processing performed through CellRanger (10X Genomics) as described in the methods section. Flow cytometry data was collected on the BD Fortessa X-20 using BD FACSDiva Software (v9.7). Microscopy data was collected on the Operetta CLS using Harmony (v4.9), the Leica STELLARIS 8 using Las X (v4.7.0.28176), and the Vectra Polaris using PhenoChart (v1.0.12) and inForm (v2.4). Supernatant analysis of cytokines was collected on the Bio-Rad Bioplex-200 using the accompanying BioManager (v6.2) software. Further details are described in the methods.
Data analysis	Analysis of single-cell transcriptomics was performed with R Statistical Framework (v4.2.1) and Python (v3.7) on an x86_64-pc-linux-gnu (64-bit) platform running under Red Hat Enterprise Linux. The following programs were also used in the bioinformatic analysis of the sequencing data: CellRanger (v6.0.2), Celda (v1.16.1) Seurat (v3), DoubletFinder (v2.3.0), Presto (v1.0.0), Destiny (v3.14.0), NicheNet (v02.01.2000) Flow cytometry data was analysed using Flowjo v10. Imaging was analysed using Harmony (v4.9), PhenoChart (v1.0.12), inForm (v2.4), Halo AI (v3.2.1851.328), KNIME (v5.2.4), CellProfiler (v4.2.5) and ImageJ (v1.54i). Non-sequencing data was plotted and analysed statistically using GraphPad Prism (v10.2.0). Sequencing data was plotted and assessed statistically in R Statistical Framework (v4.2.1).

For manuscripts utilizing custom algorithms or software that are central to the research but not yet described in published literature, software must be made available to editors and reviewers. We strongly encourage code deposition in a community repository (e.g. GitHub). See the Nature Portfolio guidelines for submitting code & software for further information.

Data

Policy information about availability of data

All manuscripts must include a data availability statement. This statement should provide the following information, where applicable:

- Accession codes, unique identifiers, or web links for publicly available datasets
- A description of any restrictions on data availability
- For clinical datasets or third party data, please ensure that the statement adheres to our policy

Sequencing files in FASTQ format supporting single cell transcriptomic analysis of homeostasis conditions as well as EpCAM TCB treatment have been deposited in ArrayExpress and are accessible at E-MTAB-14171 and E-MTAB-14170 respectively. Raw count matrices, together with metadata information, for all scRNA-seq samples discussed in this study have been deposited in Mendeley and are available at https://data.mendeley.com/datasets/5h3ym82bnb/1. Source data underlying all graphical representations used in the figures is provided as supplementary information.

Research involving human participants, their data, or biological material

Policy information about studies with human participants or human data. See also policy information about sex, gender (identity/presentation), and sexual orientation and race, ethnicity and racism.

Reporting on sex and gender	Biological material was derived from both sexes, 16 males and 11 females ranging from ages 40 - 89. Gender-based analysis was not performed - researchers were blinded to the sex and age of the donating patients at the point of experimentation. All experiments contained intra-donor controls such that donor-specific effects could be considered in the context of each biological replicate. Our findings were consistent across a diverse range of age and sex and strictly governed by variables independent of sex, namely drug treatment or location of immune cell source (blood v intestine).
Reporting on race, ethnicity, or other socially relevant groupings	Researchers were blinded to the race, ethnicity and other socially relevant groupings of the donating patients. All experiments contained intra-donor controls such that donor-specific effects could be considered in the context of each biological replicate. Our findings were consistent across all biological replicates tested.
Population characteristics	Patients underwent visceral surgery with partial resection of intestines for various oncologic indications, e.g. pancreaticojejunostomy due to pancreatic adenocarcinoma. We used micro- and/or macroscopically tumor-free regions of resectates for experiments in this study.
Recruitment	Patients undergoing surgery (e.g. pancreatic or colorectal) in academic centers donated resected tissues within the HTCR framework. The authors were not involved in recruitment, and sample selection was opportunistic for availability, amount of tissue and blood.
Ethics oversight	Human intestinal tissue samples and annotated data were obtained and experimental procedures performed within the framework of the non-profit foundation HTCR (Munich, Germany) including informed patient's consent. The framework of the HTCR Foundation, has been approved by the ethics commission of the Faculty of Medicine in the LMU (number 025-12) and the Bavarian State Medical Association (number 11142).

Note that full information on the approval of the study protocol must also be provided in the manuscript.

Field-specific reporting

Please select the one below that is the best fit for your research. If you are not sure, read the appropriate sections before making your selection.

☒ Life sciences ☐ Behavioural & social sciences ☐ Ecological, evolutionary & environmental sciences

For a reference copy of the document with all sections, see nature.com/documents/nr-reporting-summary-flat.pdf

Life sciences study design

All studies must disclose on these points even when the disclosure is negative.

Sample size	We considered one organoid to represent an intestinal unit. Each organoid experiment in the manuscript included tens to hundreds of individual organoids. Analysis of immune cell behaviour from intestinal tissue or IIO cultures was repeated on two to six biological replicates, each with two to six technical replicates (information on individual experiments is clearly stated in the figure legends). No statistical method was used to determine sample size. Instead sample sizes were determined empirically, taking into account both opportunistic availability of primary tissue and variability of results between technical experimental and biological replicates.
Data exclusions	For scRNA-seq, all data exclusion criteria were pre-established and based on standard sequencing analysis practises. Low quality cells with a low number of expressed genes or high proportion of mitochondrial gene counts or abnormal library sizes were excluded from the dataset. No additional data from any experiment was excluded.
Replication	All non-sequencing experiments presented in this study were repeated in at least three biologically-independent experiments, with the exception of figure 3c (1 biological donor in technical duplicates) and Extended Data Figure 7 (2 biological donors in technical duplicates or triplicates). Where only representative data is shown, replicated data were successful and showed similar results. This information is clearly

stated in the figure legends.
The first scRNA-sequencing experiment (figure 2) was performed after pooling at least 5 technical replicates for each experimental condition from three biological donors. The second scRNA-sequencing experiment (figure 3-4) was performed after pooling at least 5 technical replicates for each experimental condition from one biological donor. The main observations were then confirmed via flow cytometry analysis in five independent biological donors.

Randomization

Randomization was not performed. Potential covariates were controlled for by running intra-donor comparisons, using donor-matched experimental conditions treated with control molecules (non-targeting TCBs, isotype antibodies or vehicle solutions), to compare to the test conditions (EpCAM TCB, ROCKi, TNFi, Immune checkpoint inhibitors)

Blinding

Blinding was not performed. All experimental analysis contained donor-matched controls and was based on machine-derived empirical quantification (scRNA-seq, flow cytometry, cytokine quantification), not amenable to subjective operator bias.

Reporting for specific materials, systems and methods

We require information from authors about some types of materials, experimental systems and methods used in many studies. Here, indicate whether each material, system or method listed is relevant to your study. If you are not sure if a list item applies to your research, read the appropriate section before selecting a response.

Materials & experimental systems

n/a	Involved in the study
☐	☒ Antibodies
☐	☒ Eukaryotic cell lines
☒	☐ Palaeontology and archaeology
☒	☐ Animals and other organisms
☒	☐ Clinical data
☒	☐ Dual use research of concern
☒	☐ Plants

Methods

n/a	Involved in the study
☒	☐ ChIP-seq
☐	☒ Flow cytometry
☒	☐ MRI-based neuroimaging

Antibodies

Antibodies used

All antibodies, dilutions and vendor information are described in Supplementary Information Table 3.
BUV395 -CD4 BD Biosciences RPA-T4 564724 1/100,
BUV737-CD69 BD Biosciences FN50 612817 1/200,
BUV737-TCR gd BD Biosciences 11F2 748533 1/100,
BUV805-CD8 BD Biosciences SK1 612889 1/100,
BV421-Ki67 Biolegend Ki67 350506 1/100,
BV510-CD45 Biolegend 2D1 368526 1/200,
BV605-CD19 Biolegend HIB19 302244 1/100,
BV605-CD103 Biolegend Ber-ACT8 350218 1/200,
BV650-HLA-DR Biolegend L243 307650 1/100,
BV711-CD117 Biolegend 104D2 313230 1/100,
BV786-CD45RA Biolegend HI1/100 304140 1/100,
BV786-CD107a Biolegend HP-3G10 339930 1/100,
FITC-CD45RO Biolegend UCHL1 304204 1/100,
PE-TNFa Biolegend MAb11 502909 1/100,
PE-CD45RO Biolegend UCHL1 304204 1/100,
PE-CD49a Biolegend TS2/7 328304 1/100,
PE-TCR Vα7.2 Biolegend 3C10 351706 1/100,
PE-Dazzle-594-GzmB Biolegend QA16A02 372215 1/100,
PE-Dazzle-594-CD25 Biolegend BC96 302646 1/100,
PE-Dazzle-594-CD27 Biolegend M-T271 356422 1/100,
PE-Dazzle-594-TCR Vd2 Biolegend B6 3314226 1/100,
PE-Cy7-CD56 Biolegend 5.1H11 362510 1/100,
PE-Cy7-CD38 Biolegend HB-7 356608 1/100,
APC-CD39 Biolegend A15153G 328210 1/100,
APC-IFNg Biolegend 4S.B3 502511 1/100,
APC-Perforin Biolegend B-D48 353312 1/100,
Alexa Fluor 700 -CD3 Biolegend HIT3a 300324 1/100,
APC-H7 Efluor780 Fixable L/D Thermo Fisher N/A 65-0865-14 1/1000
FABP1 Life Technologies PAS28945 1/9
CD103 Abcam 224202 1/100
CD3 Ventana 790-4341 prediluted
CD4 Ventana 790-4423 prediluted
CD8 Ventana 790-4460 prediluted

CD69 Abcam ab233396 1/10
Cleaved Caspase-3 Cell Signaling Technology 9661 1/9
E-Cadherin Ventana 760-4497 prediluted

Validation

For flow cytometry, expected staining patterns of lineage-defining surface proteins were confirmed using pre-qualified control samples. Gates were set against FMO (fluoresence minus one) or unstimulated negative controls. For imaging, secondary only and isotypes controls were applied during establishments of antibody staining panels. Here, all antibodies were tested on human native tissue as validation, before staining the cultures.

Eukaryotic cell lines

Policy information about cell lines and Sex and Gender in Research

Cell line source(s)	Organoid lines and tissue-derived immune cells were derived from the healthy margin of primary tumor surgical resections. Information on the sex of the patients is listed in Supplementary Information Table 4.
Authentication	All samples were derived from primary patient tissue samples. Absolute validation was confirmed by expression of cell lineage-defining markers and transcriptomic analysis.
Mycoplasma contamination	All lines used in the studies were verified to be negative for mycoplasma before experimentation.
Commonly misidentified lines (See ICLAC register)	None.

Flow Cytometry

Plots

Confirm that:

☒ The axis labels state the marker and fluorochrome used (e.g. CD4-FITC).

☒ The axis scales are clearly visible. Include numbers along axes only for bottom left plot of group (a 'group' is an analysis of identical markers).

☒ All plots are contour plots with outliers or pseudocolor plots.

☒ A numerical value for number of cells or percentage (with statistics) is provided.

Methodology

Sample preparation	Egressed immune cells from primary tissue were harvested, stained and characterized using standard flow cytometry staining protocols (full details in the methods section). Immune cell-organoid cocultures were first digested into a single cell suspension and filtered, before being subjected to flow cytometry staining (as detailed in the methods). Samples were always acquired immediately after staining.
Instrument	BD LSRFortessa X20.
Software	FowJo v10.8.1.
Cell population abundance	No flow cytometry based sorting was performed.
Gating strategy	Viable immune cells were selected based on expression of CD45 and a viability dye. Debris and doublets were subsequently excluded based on scatter signal. Immune cell subpopulations were defined on the basis of lineage-defining markers which clearly separated populations into positive and negative expressors. For analysis of intracellular cytokines, gating was compared to and based on background expression levels in matched unstimulated control samples.

☒ Tick this box to confirm that a figure exemplifying the gating strategy is provided in the Supplementary Information.